DALHOUSIE UNIVERSITY

THE STRENGTH EVOLUTION OF A CRUSTAL SCALE SHEAR ZONE

Olivia Rolfe

SUBMITTED IN PARTIAL FULFILLMENT OF THE REQUIREMENTS FOR
THE DEGREE OF BACHELOR OF SCIENCES, HONOURS
DEPARTMENT OF EARTH SCIENCES
DALHOUSIE UNIVERSITY, HALIFAX, NOVA SCOTIA

April 2020

Distribution License

DalSpace requires agreement to this non-exclusive distribution license before your item can appear on DalSpace.

NON-EXCLUSIVE DISTRIBUTION LICENSE

You (the author(s) or copyright owner) grant to Dalhousie University the non-exclusive right to reproduce and distribute your submission worldwide in any medium.

You agree that Dalhousie University may, without changing the content, reformat the submission for the purpose of preservation.

You also agree that Dalhousie University may keep more than one copy of this submission for purposes of security, back-up and preservation.

You agree that the submission is your original work, and that you have the right to grant the rights contained in this license. You also agree that your submission does not, to the best of your knowledge, infringe upon anyone's copyright.

If the submission contains material for which you do not hold copyright, you agree that you have obtained the unrestricted permission of the copyright owner to grant Dalhousie University the rights required by this license, and that such third-party owned material is clearly identified and acknowledged within the text or content of the submission.

If the submission is based upon work that has been sponsored or supported by an agency or organization other than Dalhousie University, you assert that you have fulfilled any right of review or other obligations required by such contract or agreement.

Dalhousie University will clearly identify your name(s) as the author(s) or owner(s) of the submission, and will not make any alteration to the content of the files that you have submitted.

If you have questions regarding this license please contact the repository manager at dalspace@dal.ca.

Grant the distribution license by signing and dating below.

	March 30th, 2020
Name of signatory	Date

DALHOUSIE UNIVERSITY

Department of Earth Sciences
Halifax, Nova Scotia
Canada B3H 4R2
(902) 494-2358

DATE: 03/30/2020

AUTHOR: Olivia Rolfe

TITLE: The Strength Evolution of a Crustal Scale Shear Zone

DEGREE: Bachelor of Science CONVOCATION: May YEAR: 2020

Abstract

The brittle-ductile transition zone, the location of greatest strength in the crust, can be determined through the construction of a stress profile with depth. The profile is constrained from the calculated flow stresses for a sequence of rocks collected at different crustal depths and the frictional flow envelope for the brittle crust. Grain microstructure and texture reflects the variations in strain and temperature, and therefore flow stresses, during exhumation through the aseismic ductile regions at depth until the brittle upper region of the megathrust. Quartzite mylonites of the Lesser Himalayan Sequence were sampled along a 3 km long transect across the footwall of the Main Central Thrust (MCT) in Bhutan. The quartz crystallographic preferred orientations (CPO) were obtained through electron backscatter diffraction. The orientation maps indicate that the quartz microfabric contains two grain size populations. The large relict grains display grain boundary migration as well as a partial foam texture indicated by straightening of grain boundaries. The smaller grain population demonstrate subgrain rotation recrystallization. The quartz CPO is characterised by a Type I partial cross girdle in the *c*-axis, which corresponds to plane strain. Orientation maxima of *c*- and *a*-axes indicate a dominant rhomb <a> slip system. A grain size piezometer was applied to determine the flow stresses. These values were combined with independently determined deformation temperatures and pressures to calculate strain rates. The large grain population presented only slight variation in flow stress, but the strain rates in the middle of the shear zone were two orders of magnitude higher than at its boundary. The maximum flow stress obtained from the recrystallised grains was approximately 110 MPa, which was assumed to be the stress at the brittle-ductile transition and therefore the strongest part of the Himalayan crust. Construction of the stress envelope for the brittle regime of the crust indicates that the pore fluid pressure along the MCT of $\lambda = 0.85$ with a friction coefficient of 0.4 is required to allow slip along the thrust. However, the geothermal gradient varies across the MCT due to overthrusting of hot over colder rocks. Therefore, the generated strength profile is only applicable to the shear zone, not to the encompassing continental crust. Finally, because the calculated stresses were not effective coevally, the strength profile is actually a stress history of the shear zone.

Key Words: Crustal strength, stress profile, Brittle ductile transition zone, Main Central Thrust, Electron backscatter diffraction

Table of Contents

List of Figures

Chapter 1: Introduction

Chapter 2: Geological Background

Chapter 3: Methods

Chapter 4: Results

Chapter 5: Discussion

List of Tables

Chapter 4: Results

Chapter 5: Discussion

List of Abbreviations

Brittle-ductile transition	BDT
Electron backscatter diffraction	EBSD
Crystallographic preferred orientation	CPO
Main Central Thrust	MCT
Main Himalayan Thrust	MHT
Main Boundary Thrust	MBT
Main Frontal Thrust	MFT
South Tibetan Detachment	STD
Greater Himalayan Sequence	GHS
Lesser Himalayan Sequence	LHS
Shumar Thrust	ST
Grain Boundary Migration	GBM
Subgrain Rotation Recrystallization	SGR
Electron Backscatter Pattern	EBSP

Acknowledgements

I would like to express my deepest gratitude to my supervisor, Dr. Djordje Grujic, for his continued support during the course of this project and over the last 3 years. He made this study an invaluable learning experience, in which I found a subject matter that I am passionate about and excited to explore in my graduate studies. I have gained so much knowledge from Dr. Grujic and I thank him for his patience, time and guidance over this journey. I would also like to thank Dr. David Prior and Dr. Marianne Negrini at the University of Otago for dedicating their time to guide me through the EBSD lab work and data processing. I would also like to thank Brent Pooley, the Petrology Technician at the University of Otago, for preparing the samples for EBSD analysis.

I am sincerely grateful to the Earth Sciences Department and all the instructors who have greatly enriched my learning experience throughout my undergraduate studies. Lastly, I want to thank my amazing friends who have made my time at Dalhousie truly unforgettable.

Chapter 1: Introduction

The strength of the crust is a central aspect of geodynamics, governing tectonic regimes and seismicity in a region. The brittle regime of the upper crust expresses the effects of stress in the form of fracturing and frictional sliding, resulting in earthquakes. However, it is the deeper aseismic zone of continuous deformation that is the load bearing portion of the crust, controlling the transfer of stress to the brittle seismogenic zone (Wech and Creager 2011, Behr and Platt 2014). The ductile regime may control the slip rate of brittle faults in the upper crust (Behr and Platt 2014). Therefore, establishing the spatial distribution and magnitude of stresses imposed in the ductile crust is fundamental to understanding the strength of the crust and the interaction between seismic and aseismic domains of crustal scale shear zones.

The spatial distribution of differential stresses through the lithosphere is primarily inferred from the results of laboratory experiments and geophysical analysis. Extrapolation of these laboratory experiments to natural conditions demonstrate that peak stresses through the crust reside in the brittle-ductile transition (BDT) zone (Sibson 1983, Behr and Platt 2014). The shift from brittle deformation by frictional sliding to ductile deformation occurs when temperature and strain rate for a given mineral and grain size reach the conditions for crystal-plastic flow (Kirby 1980, Scholz 1988). Behr and Platt (2011) combined field observations from the Whipple Mountains metamorphic core complex coupled with thermobarometry, paleopiezometry and thermal modelling to constrain a strength profile through the middle crust. A strength profile provides insight to the conditions of deformation and the location BDT zone (Figure 1.1), displaying the variations in differential stress with depth and temperature through the lithosphere.

The brittle and ductile deformation regimes display two different strength profiles. Deformation through the ductile lower crust follows a ductile flow law, such as the quartz flow law determined by Hirth et al., (2001). This flow law produces a flow curve as flow stresses in this domain are non-linearly dependent on temperature, grain size and strain rate.

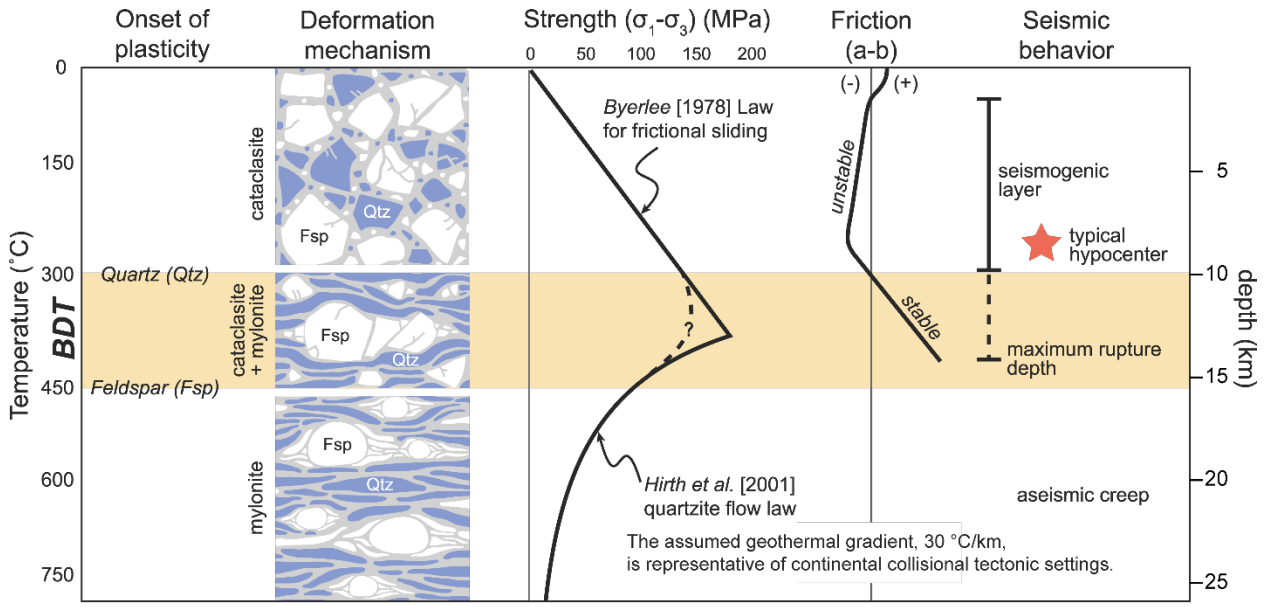

Figure 1.1. The rock deformation mechanisms and associated stress profile with increasing depth in a continental collisional tectonic setting. The brittle ductile transition zone is highlighted in yellow. Modified from Nevitt et al. (2017).

Strain that accumulates in the lithosphere is partitioned and localizes into shear zones. Stress through shear zones in the brittle upper crust follows Byerlee's law. This law produces a linear relationship between differential stress and the effective normal stress through the coefficient of friction, which is described by the Coulomb frictional failure criterion. The coefficient of friction (μ_f) is determined by the expression:

$$\mu_f = \frac{\sigma_s}{\sigma_n} \quad (1)$$

Where σ_s is critical shear stress required to activate slip on a fracture and σ_n is the normal stress acting across the fracture (Fossen 2016). These high-strain zones with continuous slip load the stress at the base of the brittle seismogenic zone that eventually fail by seismic slip, some of which causing mega-earthquakes (Sibson 1982). Geophysical investigation provides increasingly precise insight into slip processes along the brittle regime of mega shear zones in which these mega-earthquakes (≥8.4 magnitude) occur (i.e. Rogers 2007). However, direct observation and accessibility to rocks of the ductile regime is scarce. Intercontinental mega thrusts provide one of the few localities to directly observe ductilely deformed rocks in mega

shear zones. The Main Central Thrust (MCT) zone of the Himalayan orogen is a relict segment of seismically active intracontinental mega thrust (Figure 1.2). The MCT exposes the rocks that have been deformed through ductile deformation during the Miocene at depths between about 10 and 40 km (Searle et al. 2008, Avouac 2015). The mylonites of the MCT zone provide a unique opportunity to observe the microstructure and study deformation mechanisms of an active megathrust in a rheological range between ductile to brittle-ductile transition.

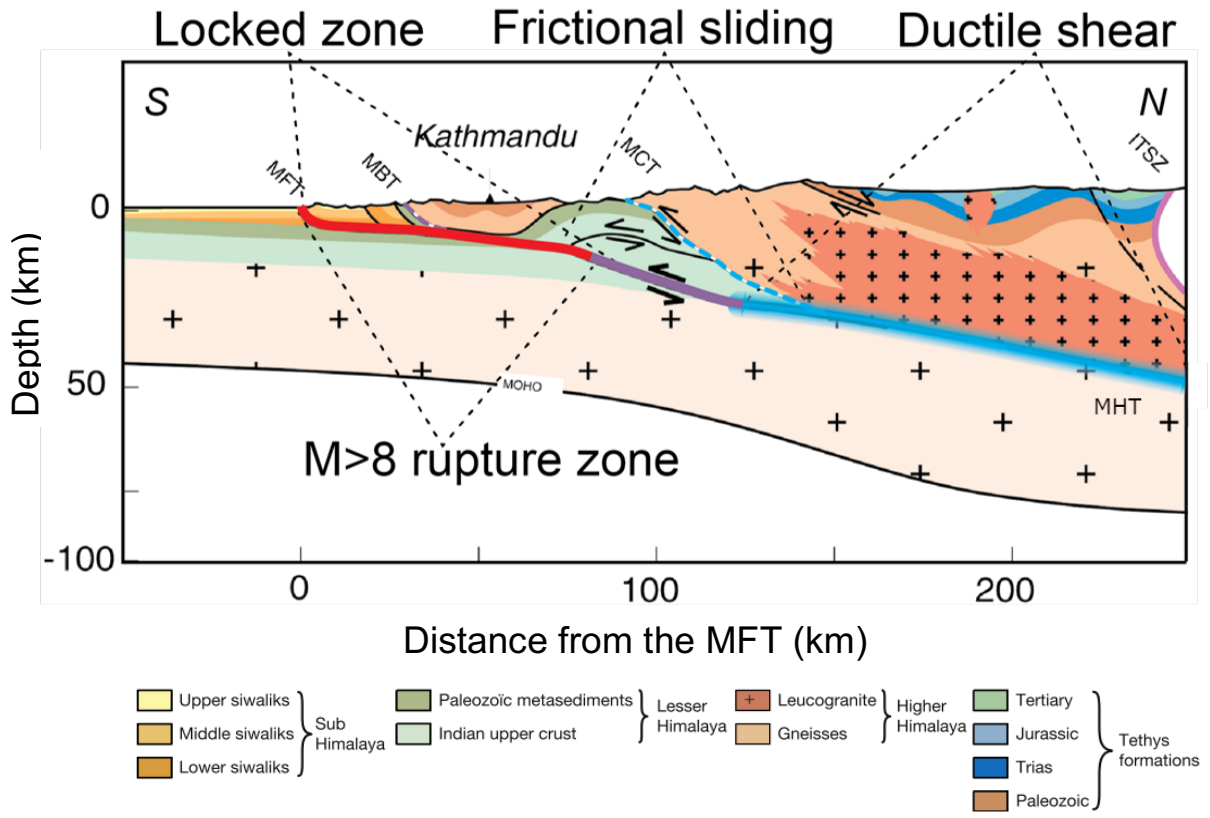

Figure 1.2. A schematic cross section of the Main Himalayan Thrust in central Nepal. The region of the ductile deformation and the Main Central Thrust highlighted in blue. The brittle-ductile transition zone is shown in purple and the brittle regime in red. Modified from Avouac (2015).

During exhumation, rocks in the shear zone are progressively cooling and thus passing through different deformational regimes. These can be identified by overprinting dynamic recrystallisation mechanisms, bimodal grain size distribution, and potentially different

crystallographic preferred orientation (CPO) patterns. Therefore, if the temperature history is known, one can construct the stress profile evolution in time.

The main aim is to obtain the peak ambient stress of the BDT in this shear zone. i.e., the strongest part of the detachment which may control the level of stress loading of the seismic zone. The peak stress at the BDT can be estimated by the construction of a stress profile though the crust of the Himalayan orogen. A stress profile was constrained by calculating the flow stresses during ductile deformation for a sequence of quartz mylonites collected across the footwall of the MCT shear zone. In addition, the stress conditions for frictional sliding along the brittle, seismic, segment of the MHT was determined. This objective was achieved by measuring grain size and microstructure of the mylonites which is a function of the variations in pressure and temperature, and therefore flow stresses. The grain size was extracted from grain maps which were constructed from crystallographic preferred orientations of quartz grains obtained through electron backscatter diffraction (EBSD) analysis. Patterns of CPOs in stereographic projection reflect the dominant deformation mechanisms, which depend on temperature, strain rate and flow stress, and can be used as proxies of deformation temperature. Independently determined deformation temperatures (Grujic et al. 2020) were used for the calculation of flow stresses. The CPOs in quartz corroborate the constructed strength profile to provide a holistic constraint on the stress through the crust and time.

Our determined strength profile of the footwall will contribute to the cumulative understanding of stress through the Main Central Thrust and the ductile regime of the Main Himalayan Thrust. By determining the peak strength in the thrust zone, one could ascertain the largest earthquake that would have occurred in the MCT during active slip. This research could provide insight regarding the processes at depth and seismicity along the currently active Main Frontal thrust (Bilham 2019).

Chapter 2: Geological Background

2.1 Regional Geology

2.1.1 Tectonic Setting and the Main Himalayan Thrust

The ongoing Himalayan orogeny began with the collision of the Indian and Eurasian Plates between 55- 50 million years ago during the Cenozoic (Najman et al. 2010). The Himalaya are composed of four major fault and shear zones, separating a series of orogen parallel litho-tectonic units parallel to the orogen (Gansser 1964, Hodges 2000, Avouac 2015). These major shear zones, structurally from South to North, are the Main Frontal Thrust (MFT), the Main Boundary Thrust (MBT), the Main Central Thrust and the South Tibetan Detachment (STD) (Figure 2.1). The four tectono-stratigraphic packages of the Himalaya, that span the length of the entire orogen, were originally defined by Heim and Gansser (1939) and Gansser (1964). These zones are the Subhimalayan zone, the Lesser Himalayan Sequence (LHS), the Greater Himalaya Sequence (GHS), and Tethyan Himalayan zone. The Subhimalayan zone is composed of deformed syn-orogenic foreland sediments, while the Lesser Himalaya Sequence, Greater Himalaya Sequence and Tethyan Sedimentary Sequence are comprised of pre-orogenic sedimentary and igneous rocks of Greater India and its northern continental margin (Hodges 2000, Yin 2006). The LHS and GHS display an inverted metamorphic sequence, from lower greenschist to upper amphibolite facies, with increasing grade structurally up section towards the North (Hodges 2000).

The Subhimalayan zone consists of unmetamorphosed Neogene sedimentary rocks of the Siwaliks group (Burbank et al. 1996, Najman 2006). The Siwalik group rocks are thrust over sediments of the active foreland basin of the Himalaya along the seismically active Main Frontal Thrust (Avouac 2015). The MBT is a north dipping brittle top to the south fault zone that places the Lesser Himalayan Sequence over the Siwalik group. The Great Himalayan Sequence Mid Proterozoic to Paleozoic rocks are emplaced over the LHS Mid Proterozoic metasediments by the Main Central Thrust, a several kilometer thick ductile shear zone (Gansser, 1994; Martin, 2017; Searle et al., 2008). Finally, on the northern margin of the thrust belt lies the Tethyan Sedimentary sequence of Paleozoic to Mesozoic unmetamorphosed to low grade sedimentary

rocks (Starnes et al., 2020). This package is separated from the GHS by the South Tibetan Detachment system, a ductile shear zone exhibiting north directed normal faulting. The MCT and STD display coeval movement over an extended period of time, from c. 25 Ma to 5 Ma (Godin et al., 2006). The MFT, MBT and MCT converge at depth into the north dipping basal detachment (Nelson et al. 1996). the Main Himalayan Thrust (MHT), which is the basal detachment of the Himalaya, prompting the under thrusting of India below southern Tibet. The megathrust transitions from brittle deformation in the upper crust to ductile deformation at depth (Avouac, 2015).

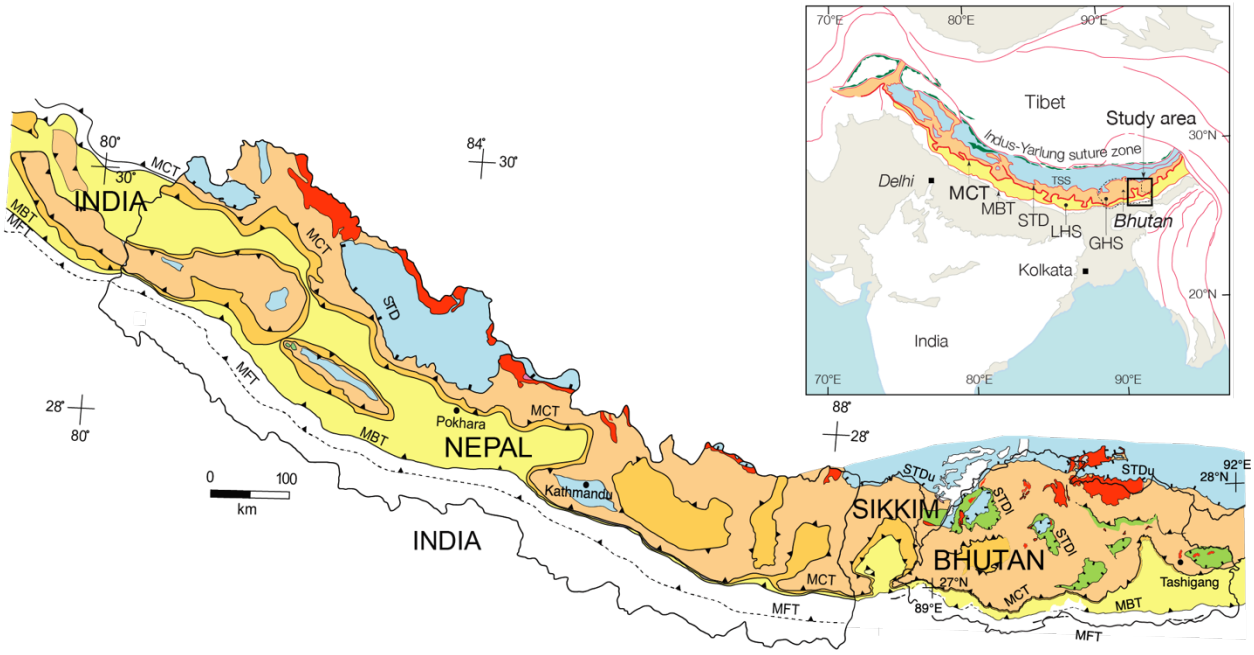

Figure 2.1. Geological map of the Himalayan orogen after McQuarrie et al. (2008). Simplified tectonic map of the Himalaya and Tibet after Gansser (1983).

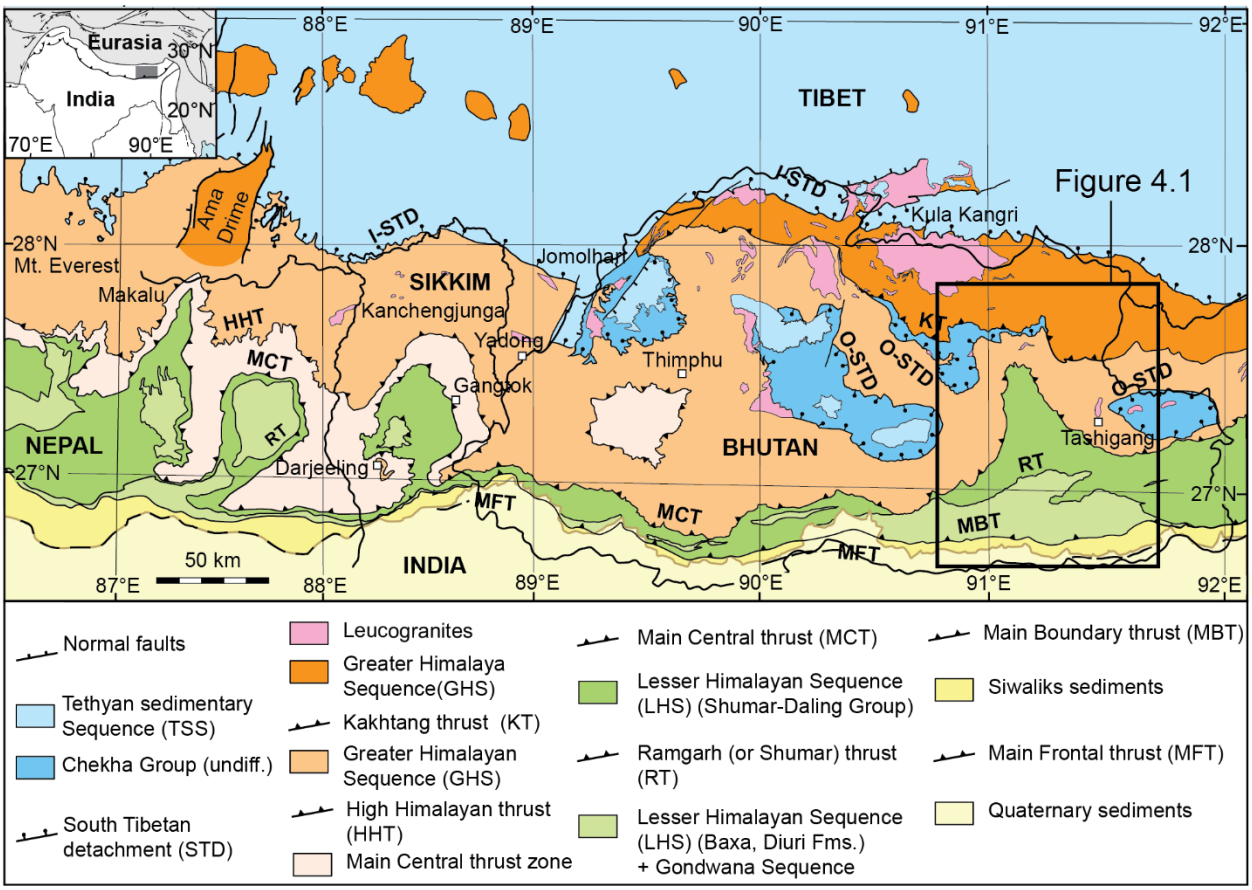

Figure 2.2. The geological map of the eastern Himalaya, modified from Grujic et al. (2011). The black square outlines the sample area shown in greater detail in Figure 4.1.

2.1.2 Geology of the Main Central Thrust Zone

The Main Central Thrust is considered one of the largest ductile shear zones of any active collisional mountain belt (Searle et al. 2008). It is a south-vergent, north-dipping thrust, with a top-to-the-south sense of shear. The crustal scale shear zone spans approximately 2,200 km along strike, cropping out from the Indian State of Jammu in the west and Kashmir to Arunachal Pradesh in the east. The MCT was the principal thrust in the Himalayan Orogen, active during the Miocene for approximately 12 million years, from ~23 Ma to ~10 Ma (Godin et al. 2006, Martin 2017a). It places the higher-grade crystalline rocks of the Greater Himalayan Sequence over the lower-grade footwall rocks of the Lesser Himalayan Sequences (Searle et al. 2008).

The Lesser Himalayan Sequence consists of greenschist facies Precambrian to Paleozoic metasedimentary rocks and is divided into two subgroups, the lower and upper Lesser Himalaya which are separated by the Shumar Thrust (ST). The upper Lesser Himalaya units from structurally lowest to highest are the Gondwana Succession, the Diuri Formation, and the Baxa Group (Long et al. 2011). Sandstones, siltstones, shales and coal comprise the Permian Gondwana succession, which is in contact with the brittle MBT at its lower bounds. The succession is overlain by the 2-3 km thick Carboniferous-Permian Diuri formation of pebble-clast diamictite and slates (Gansser 1983, McQuarrie et al. 2008). The Proterozoic-Cambrian Baxa Group lies structurally above the Diuri Formation. This unit contains quartzite, metasiltstone and slate with massive beds of dolomite and limestone (McQuarrie et al. 2008). At its top, the Baxa Group is bordered by the Shumar Thrust, separating it from the overlying Daling Formation.

The stratigraphically lower Lesser Himalaya is composed of the Mid Proterozoic Daling-Shumar Group. The Daling Formation is a succession of interlayered quartzites, phyllites and schist with segments of the Mid Proterozoic granitic gneiss and carbonates (Daniel et al. 2003, Long et al. 2011a). The Shumar Formation consists primarily of medium to thick bedded quartzite interlayered with schist and phyllite along with lenses of mylonitic Mid Proterozoic granitic gneiss (Long et al. 2011). The lithologies present in the Shumar Formation allow for observations of quartz microstructures along a significant structural distance across the thrust zone. The Jaishidanda Formation, a thin litho-tectonic unit between the LHS and GHS, lies above the Shumar Formation, consisting of garnet-biotite schist and biotite rich quartzites (Dasgupta et al. 1995, Daniel et al. 2003). The Jaishidanda Formation as well as the Daling-Shumar Group lie within the mylonitic belt of the MCT shear zone that extends downwards for approximately 3 km.

The Greater Himalayan Sequence ranges from 10 to 30 km in thickness, comprising the metamorphic core of the Himalayan orogen (Law et al. 2013). It is composed of granitic orthogneisses with intervals of metasedimentary units interbedded with schist, migmatites and Miocene leucogranites (Daniel et al. 2003).

Metamorphic index minerals of the MCT display a zone of inverted metamorphic isograds, increasing northward and structurally upwards from biotite grade to sillimanite grade, initially mapped by Gansser (1983). The greatest portion of this metamorphic zone lies in the Lesser Himalayan Sequence. In eastern Bhutan the LHS contains three metamorphic isograds, a lower greenschist facies isograd along the Main Boundary Thrust, a higher greenschist facies isograd in the Baxa Group and a biotite facies isograd within the Jaishidanda Formation near the MCT (Gansser 1983). The mineral assemblage of the biotite facies isograd is garnet + biotite + muscovite + plagioclase + quartz (Daniel et al. 2003).

Shortening and stacking of the LHS rocks resulted in the development of two overlapping duplexes, the Daling and Rangit (Landry et al. 2016). The Daling Duplex developed during the formation of its roof thrust, the MCT zone and is bounded by the MBT at the bottom. The Rangit duplex incorporates the Daling, Baxa and Gondwana units, in the eastern Bhutan it has a geometry of a hinterland dipping duplex with about eight horses (Long et al. 2011a). The MBT forms the floor thrust and the Shumar Thrust forms the roof thrust (Landry et al. 2016).

There are many conflicting definitions of the MCT and of its location (e.g. Yin 2006, Searle et al. 2008, Martin 2017b), as the thrust is not only a shear zone but also a major protolith boundary and is associated with an inverted metamorphic field. Therefore, the definition of the MCT has both structural, paleogeographic and metamorphic implications. The boundary of a shear zone, which is several kilometres wide, is determined based on the strain gradient from undeformed rocks outside of the shear zone to rocks of increasingly higher strain towards the centre of the shear zone (Larson et al. 2017). The boundary between undeformed and deformed rocks is diffuse and therefore subject to individual interpretation in the field. The mylonitic belt in the footwall and hanging wall block of the MCT is observed over several kilometres, with heterogenous strain and variable degrees of mylonitization (Larson et al. 2017, Long et al. 2016, Starnes et al. 2020). The inconsistent definitions of the MCT cause variations in the interpretation of the MCT location over a structural distance of up to 5 km (Martin 2017a). In the Bhutan Himalaya, the mapped MCT is recorded at the contact between the GHS and the Jaishidanda Formation. However, we adhere to the definition of the MCT presented by Long et

al. (2012) in which the MCT extends to the edge of shearing rather than being constrained to the protolith boundary.

The MCT is crucial to our understanding of relationship between different deformation regimes along the Main Himalayan Thrust as it exhumes rocks from the ductile deformation regime of the MHT, exposing them for physical analysis. Microstructures of quartz mylonites of the LHS provide fundamental insight into the kinematic and mechanical properties of rocks during deformation below the brittle-ductile transition zone. By sampling rocks across the MCT shear zone, from the core (the protolith boundary) to the shear zone boundary in the footwall block we can examine trends with increasing structural distance from the shear zone. The microstructure of the mylonites may also register changes in the mechanical properties as the rocks were exhumed and cooled from the peak deformation temperatures to the brittle ductile transition zone.

2.2 Microstructures of Quartz

In order to produce a stress profile, we must determine the ductile behaviour of quartz in the sampled mylonites. Ductile deformation is facilitated by lattice defects and their movement through crystals as stress is applied (Fossen 2016). Lattice defects are irregularities in the crystal structure that can be grouped into two categories, point defects and dislocations. Point defects are extra or missing atoms in the crystal lattice (Passchier and Trouw 2005). Diffusion creep is a form of deformation in which vacancies within the crystal lattice migrate (Passchier and Trouw 2005). Dislocations are linear defects in the crystal lattice in which there are two main types, edge and screw dislocations (Figure 2.3). Edge dislocations form as a result of an extra half lattice plane present within the crystal structure. Screw dislocations are oriented parallel to the slip direction, caused by a section of the crystal that is displaced over one lattice distance producing a lattice plane that is twisted (Bestmann and Prior 2003, Passchier and Trouw 2005).

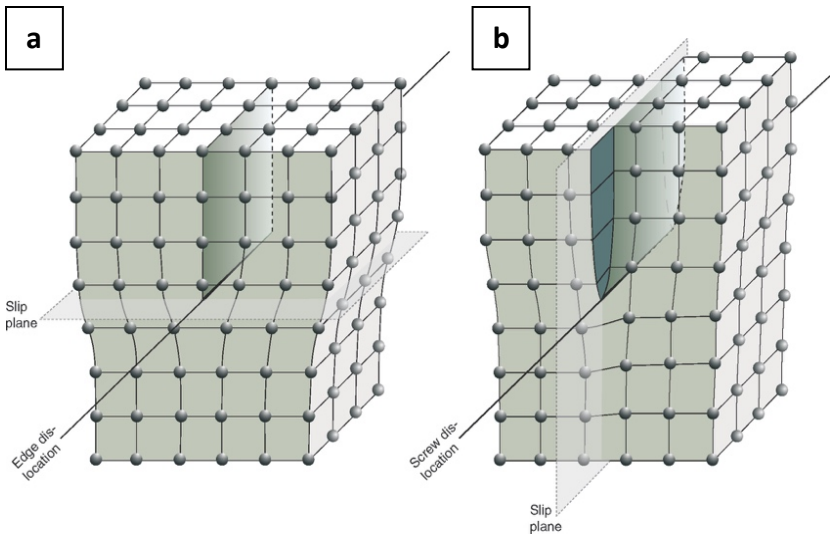

Figure 2.3. The two types of dislocations. a) An edge dislocation with an extra half lattice plane and b) a screw dislocation with a twisted lattice. From Fossen (2016).

Dislocations contribute to intracrystalline deformation by slip, a mechanism in which there is a slip plane with a dislocation front that propagates. Ductile deformation in rocks is achieved primarily by dislocation glide and dislocation creep, through the movement, formation and destruction of these dislocations (Fossen 2016). The Burgers vector characterizes the direction and minimum amount of lattice displacement resulting from a dislocation. Slip planes and slip directions (Burgers vector) within a crystal lattice are activated by applied stress. Temperature dominates the critical amount of stress required for slip and determines the crystal-plastic deformation mechanism (Figure 2.4). Therefore, ascertaining the mechanisms of deformation can inform on the conditions at which deformation occurred.

Dislocation creep reduces the internal energy of grains through the movement of dislocations along grain boundaries or concentrating dislocations in an area. This movement of dislocations to reduce internal energy creates recovery textures in quartz (Passchier and Trouw 2005). The areas of high dislocation densities yield slight variations in orientation within the grain that is distinct under the microscope. Undulose extinction in quartz is caused by the organization of dislocations into dislocation walls. (Fossen 2016). Subgrains are another form of

recovery. They are produced by dislocation alignment into planar domains ("walls") within the grain, developing dislocation free patches (Figure 2.5) (Fossen 2016).

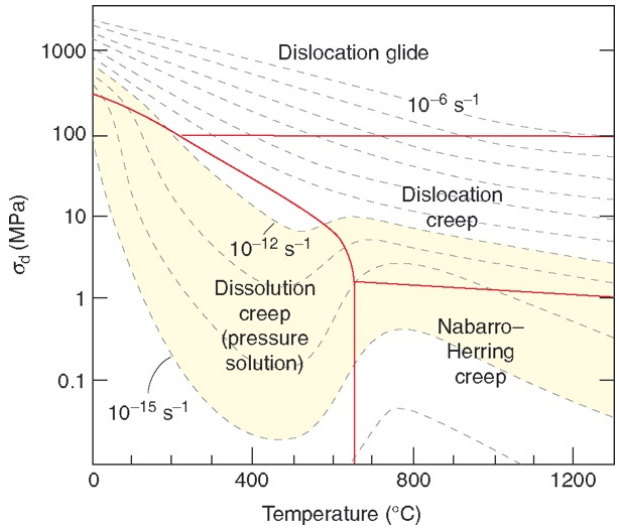

Figure 2.4. Deformation mechanism map for quartzite with 0.1 mm grain size. From Fossen (2016).

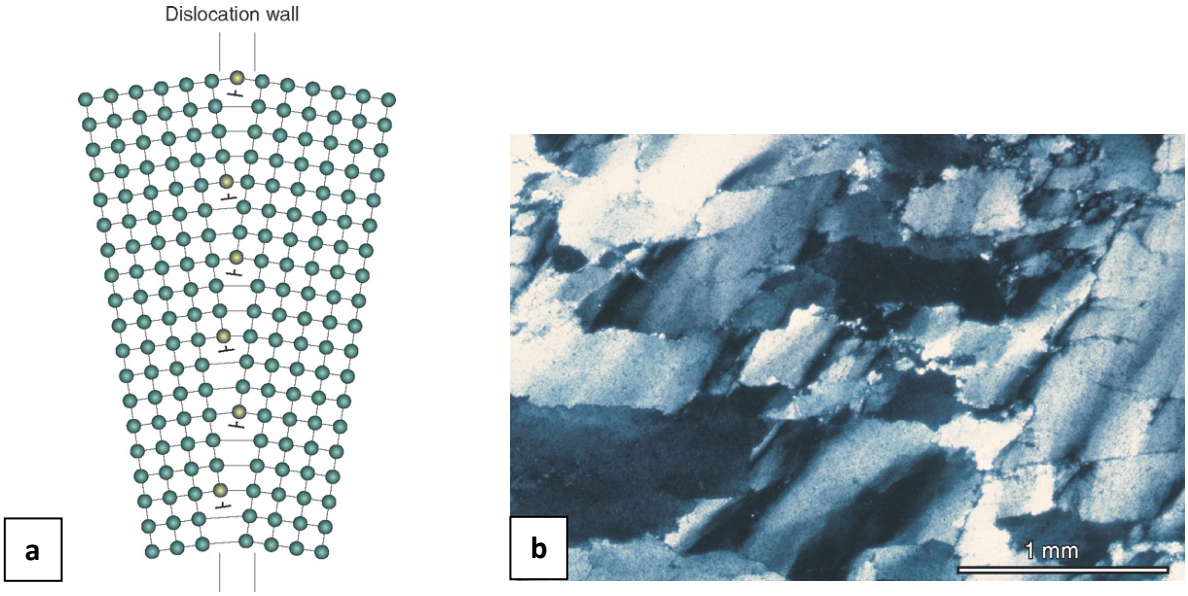

Figure 2.5. a) A dislocation wall comprised of edge dislocations. From Fossen (2016). b) Undulose extinction in quartz showing the concentration of dislocations into dislocation walls.

Recrystallization occurs when recovery continues to the point of removing all the dislocations within a grain, making it strain free (Passchier and Trouw 2005). There are three principal mechanisms of dynamic recrystallization in quartz (Figure 2.6): grain boundary migration (GBM), subgrain rotation recrystallization (SGR) and bulging recrystallization (BLG) (Hirth and Tullis 1992). These mechanisms are less discernible in partially and completely recrystallized fabrics than deformation or recovery textures, however they provide key indications of the pattern of recrystallization within the rock and relationship to the relict grains.

The three mechanisms of dynamic recrystallization in quartz are a function of the temperatures and strain rates, and therefore the stresses the rock is subjected to, operating at discrete intervals of these parameters. The mechanisms provide semi-quantitative deformation thermometers. Stipp et al., (2002) correlated experimentally derived dislocation creep regimes and the microstructures in quartz associated with the mechanisms of dynamic recrystallization observed in the field with well-known metamorphic temperatures to determine the temperature intervals at which these mechanisms occur. Stipp and co-workers concluded that bulging develops between temperatures of ~280 to ~400 °C, subgrain rotation recrystallization between an interval of ~400 to 500 °C, with the transition to grain boundary migration at ~500 °C. These temperature windows correspond to quartzites of the eastern Tonale Fault zone however, they can be applied as an estimate to the temperatures of dynamic recrystallization mechanisms in naturally deformed quartz in other localities.

In grain boundary migration recrystallisation grain boundaries of strain free grains migrate into neighbouring grains with higher dislocation densities and therefore higher energies. Because of this, GBM textures primarily display one grain growing at the expense of another. GBM produces low energy grains with lobate and curved grain boundaries, removing dislocations and subgrains (Passchier and Trouw 2005). Under increased temperatures grains can show highly amoeboid boundaries, presenting an essentially “strain free” grain. Jessell (1987) proposed the primary microstructures of GBM and the methods for determining the

movement direction of grain boundaries. There are four distinctive textures resulting from GBM which indicate the direction of movement, including window texture, pinning, left-over grain texture and dragging (Figure 2.7).

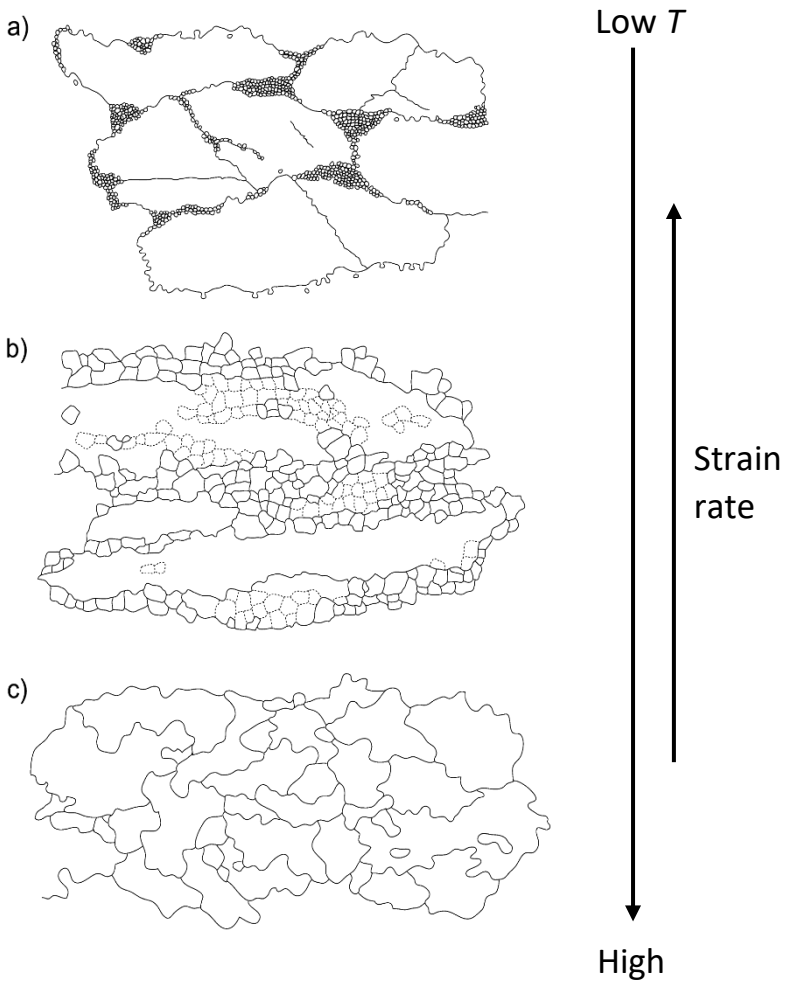

Figure 2.6. The microstructures of the three dominant mechanisms of dynamic recrystallization in quartz, a) bulging, b) subgrain rotation and c) grain boundary migration, with their correlation to temperature and strain rate. Modified from Stipp et al. (2002).

Window texture develops by the migration of quartz grain boundaries into a gap between two mica grains. This texture displays the direction of movement of the grain boundary into another quartz grain between the mica "window", Figure 2.7.a (Passchier and Trouw 2005). Pinning texture (Figure 2.7.b) forms from the movement of grain boundaries being restricted by mica grains present either between grains or as inclusions within the higher

energy quartz grain. This yields a distinct variation in curvature of the quartz grain boundaries surrounding the second phase grain. Pinning is the simplest form of GBM (Jessell 1987) and often the most commonly observed.

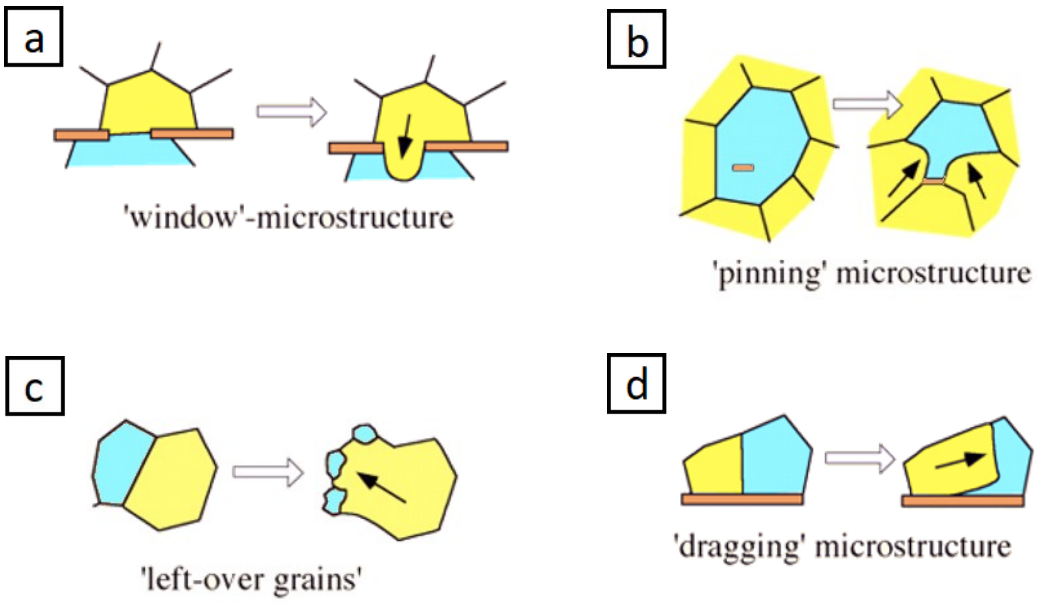

Figure 2.7. Four microstructures of grain boundary migration that indicate the direction of grain boundary movement, shown by the solid black arrow. The blue grains represent higher energy quartz grains with high dislocation densities. The yellow quartz grains are strain free. Secondary phases are shown in orange. From Passchier and Trouw (2005).

Isolated grains with identical orientations are remnants of a larger grain following the almost complete consumption of this grain by its neighbour (Figure 2.7.c). These remnant grains comprise a “left over grain” texture; their relative positions indicate the direction of grain consumption and boundary migration (Jessell 1987). Of the four microstructures that reveal the direction of GBM, this is the sole texture that does not require the presence a second phase mineral (i.e. muscovite). For a dragging texture to ensue, two quartz grains must first be pinned by a mica grain. The quartz-quartz grain boundary exhibits a sharp deflection near the triple junction between the three grains, creating an acute angle (Jessell 1987). The acute angle points toward the quartz grain growing at the expense of its neighbour (Figure 2.7.d)

Subgrain rotation recrystallization develops as dislocations are added continuously to subgrain boundaries within a quartz grain due to stress. This results in the progressive misorientation of the subgrains as the angle on either side of the crystal lattice increases (Passchier and Trouw 2005). In classifying grain boundaries, we considered sub grains to have misorientation angles between 5 ° and 10 °, termed low angle boundaries. Eventually, these low angle boundaries evolve into high angle boundaries, with misorientation angles becoming significant enough ($\geq 10\ °$) that the subgrains can be considered new recrystallized grains. Typically, recrystallized grains form rims surrounding lenses of the relict grains (Figure 2.6.b). This is considered a core and rim texture or a mosaic texture in metamorphic petrology. However, with enough time and strain the formation of new grains can completely overprint the initial grains.

The third mechanism of dynamic recrystallization, bulging, occurs at low temperatures (280 to 400 °C) in which the mobility of grain boundaries is restricted to localized areas along boundaries. Slight migration of grain boundaries into neighbouring grains with higher dislocation densities produces small new grains (Figure 2.6.a) (Passchier and Trouw 2005). These bulges may initially develop as subgrains before progressing to new crystals. The new grains occur primarily at triple junctions and along the boundaries of old grains (Passchier and Trouw 2005).

2.3 Crystallographic Preferred Orientation Pole Figures

The crystal lattices of minerals in a ductilely deformed rock are arranged in a systematic manner, creating a crystallographic preferred orientation (Passchier and Trouw, 2005), or lattice preferred orientation. The CPO pattern is controlled by the deformation mechanisms, temperature, strain geometry and strain rate active during ductile flow (Little et al. 2015). Therefore, the CPO patterns present are indicative of the flow stresses and variations in CPO patterns reflect changes in these flow stresses during deformation (Heilbronner and Kilian, 2017). The Flinn diagram (Figure 2.8) illustrates the relationship between the CPO patterns in the *c*- and *a*- axes and finite strain. The patterns present can be used to infer the principal form of strain (Stipp et al. 2002).

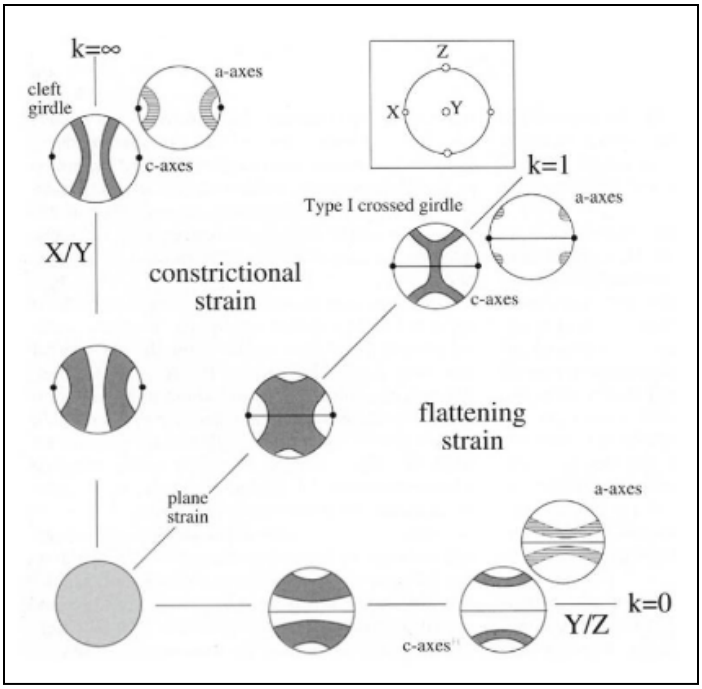

Figure 2.8. The Flinn Diagram, relating strain type to CPO patterns in the *c*-axes (dark grey) and *a*-axes (light grey). From Passchier and Trouw (2005).

At lower temperatures (<500 °C) the *c*-axis displays cross girdle fabrics, while at high temperatures maxima in the *c*-axis are located on the periphery (Stipp et al., 2002). Cross girdle fabrics in quartz are displayed in Figure 2.9 with Type I cross girdles defined by two small circles about the y axis, connected by a girdle. Type II cross girdles form an X shape through the centre of the CPO. The dominant slip system of deformation can be surmised based on the location of the maxima present in the pole figures (Figure 2.10). Maxima in the periphery represent deformation by basal <a> slip. Rhomb <a> slip is dominant when maxima lie between the centre and the periphery of the CPO. At higher temperatures, (~550 °C) prism <a> slip operates, with maxima in the centre of the CPO (Okudaira et al. 1995). Strong and consistent flow patterns during deformation result in stronger, more distinct CPO patterns (Toy et al. 2008). Obscure patterns suggest deformation under weak flow stresses or variations in flow stresses. The strength of a CPO pattern is dependent on the percentage of grains oriented parallel to the fabric skeleton and the percentage of dispersion around it. CPO strength is reflected by the

contours present and the multiple uniform density (MUD) which is the frequency of the occurrence of a given orientation.

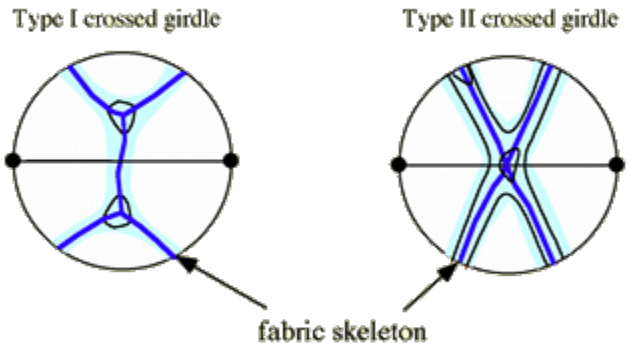

Figure 2.9. An example of Type I and Type II cross girdles of the *c*-axis of quartz CPOs. From Passchier and Trouw (2005).

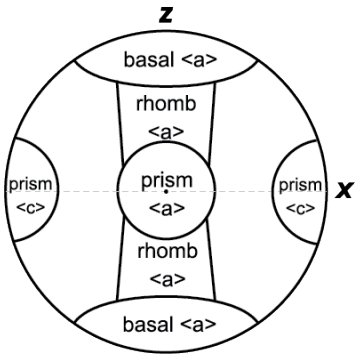

Figure 2.10. The locations of maxima in the *c*-axis of CPO figures and the dominant slip system in quartz. X is the direction of lineation and Z is perpendicular to the foliation. From (Toy et al. 2008)

Chapter 3: Methods

3.1 Sample Collection and Preparation

The six quartz mylonite samples were collected from the Shumar unit of the LHS in the footwall of the Main Central Thrust (MCT) in eastern Bhutan by Professor Djordje Grujic. The sampling sites were located along the exposed roadside, taken along two transects spanning a structural distance of ~3 km, shown in Figures 3.1 and 3.2.

Thin sections for optical petrography and EBSD were cut in the kinematic reference frame, perpendicular to the macroscopic foliation and parallel to the lineation of the rock (Halfpenny 2010). Six rock chip samples for EBSD were prepared into polished thin sections. EBSD samples are required to be "super polished" as the orientation of the grains is analysed at surface of the crystal (Passchier and Trouw 2005). Normal polishing techniques often damage the surface of the specimen, negatively affecting the resulting EBSP pattern. Final polishing was performed using a vibratory polisher with colloidal silica, which provides a uniform and damage free sample surface (Halfpenny 2010).

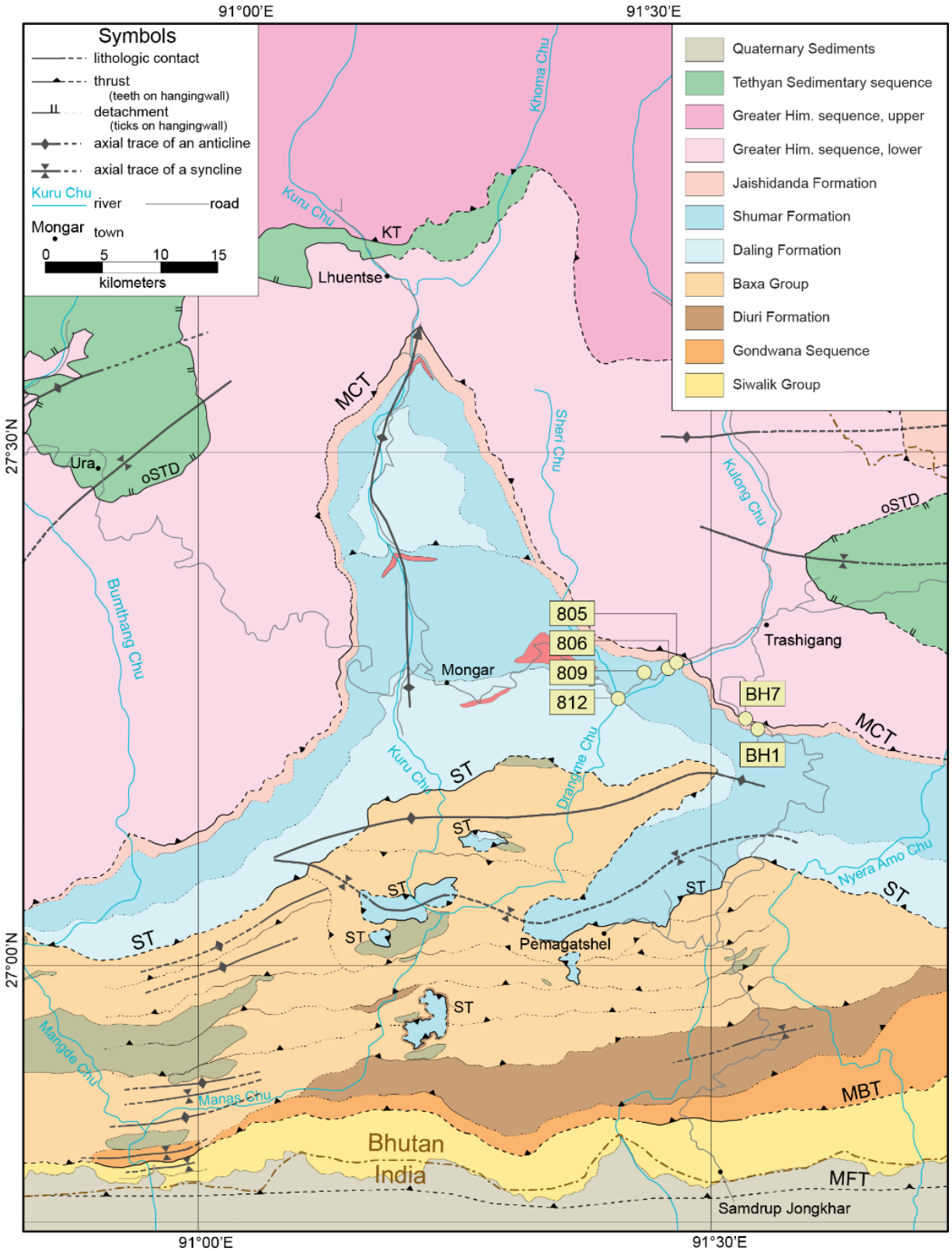

Figure 3.1. Geological map of eastern Bhutan, illustrating the sampling locations along the footwall of the MCT in the Shumar unit. After Long et al. (2011)

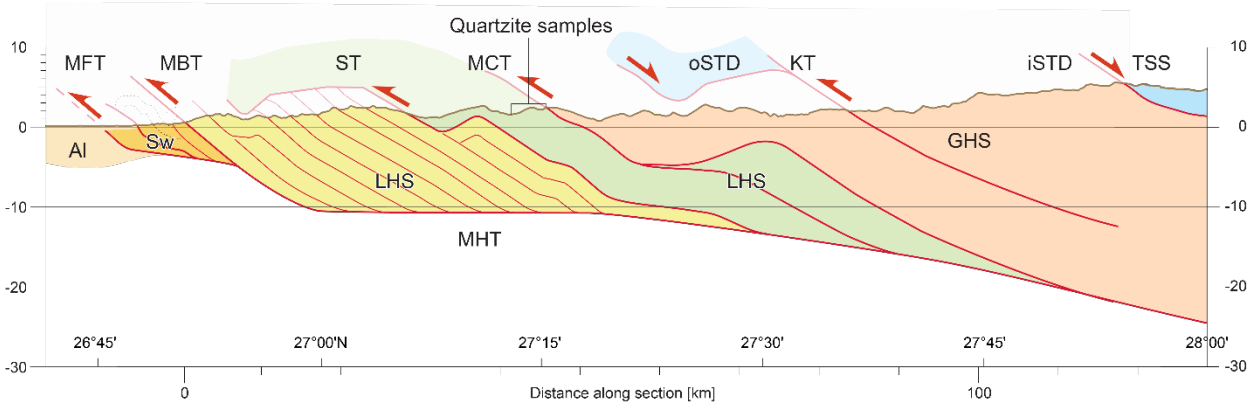

Figure 3.2. The Structural cross section of the Himalayan orogen in eastern Bhutan along ~91.5 °E. Abbreviations of lithologies south to north: Al - Alluvium, Sw – Siwalik Group, LHS- Lesser Himalayan Sequence, GHS - Greater Himalayan Sequence, and TSS - Tethyan Sedimentary Sequence. Structures: MFT- Main Frontal Thrust, MBT- Main Boundary Thrust, ST – Shumar Thrust, MCT- Main Central Thrust, oSTD and iSTD – outer and inner South Tibetan Detachment, KT- Kakhtang Thrust, MHT- Main Himalayan Thrust. Modified from Long et al. (2011).

3.2. Electron Backscatter Diffraction

Electron backscatter diffraction is a textural analysis technique used to obtain the crystallographic preferred orientation of minerals. The EBSD detection method utilizes a scanning electron microscope (SEM) which directs an incident beam of accelerated electrons at the sample. The accelerated electrons backscatter at slight angles to the lattice planes within a crystal, producing varying bands of intensities called Kikuchi bands or electron beam scattering patterns (EBSP). A diffraction pattern composed of the Kikuchi bands is captured onto a phosphor screen and registered by the EBSD camera (Figure 3.3.a). The positions of the Kikuchi bands (Figure 3.3.b), which correspond to the geometry of the lattice planes and their d-spacings (distance between lattice planes), are identified through the Hough transform routine (Adams et al. 1993). The angles between the detected bands are calculated and compared to the known interplanar angles for the structure of interest, in this case quartz, automatically indexing the diffraction patterns.

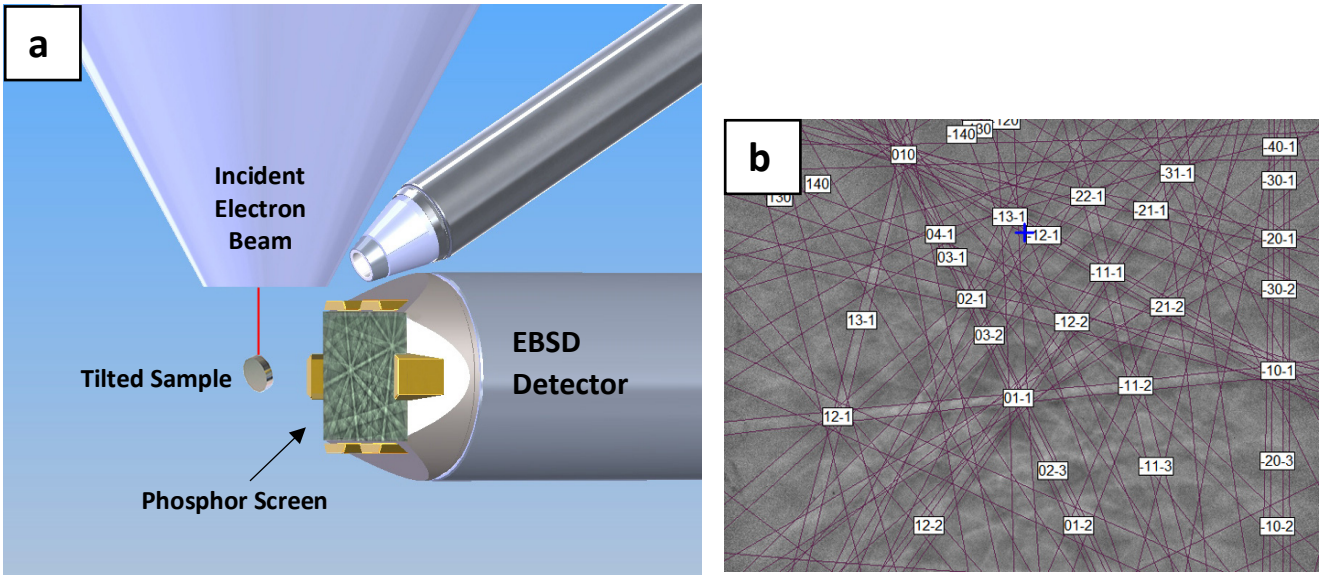

Figure 3.3.a) A schematic of the SEM chamber and the relation of the sample to the EBSD detector. The diagram illustrates the generation of the Kikuchi bands from the backscattered electrons (modified from Oxford Instruments, 2015). b) Indexed Kikuchi bands produced from the electron backscatter diffraction pattern of quartz (Oxford Instruments, 2020).

Analysis of quartzite samples by EBSD was conducted at the Otago Centre for Electron Microscopy (Figure 3.4) at the University of Otago in New Zealand. Imaging was performed with a Zeiss Sigma VP Field Emission Gun Scanning Electron Microscope fitted with a NordlysF EBSD camera. The EBSD data were collected with an EHT current (accelerating voltage) of 30.0 kV, aperture of 300 µm and current of 58.8 nA. The samples were tiled at 70 ° with a working distance of ~30 mm. Operated with *AZtec* software by Oxford Instrument, the EBSD camera was set to a binning mode of 2x2, gain of 12 and an exposure time of 3.7 ms. A polished section of each sample was initially mapped with a 20 µm step size. Detailed runs of selected areas within each thin section were conducted with a step size of 2µm. The *Aztec* software automatically indexed the diffraction patterns against its reference database. The orientation data was plotted as grain maps and exported to be processed using the *HKL Channel 5* program by Oxford Instruments.

Figure 3.4. The SEM lab at the Centre for Electron Microscopy at the University of Otago.

3.3 Orientation Maps

Orientation grain maps were reconstructed with each grain defined as a region with the same crystal orientation and the boundaries of each grain defined by a critical misorientation angle. Orientations that differ by this critical angle or greater are considered separate grains. Quartz grain boundaries were established by a minimum misorientation angle of 10 ° and subgrain boundaries were defined by a minimum misorientation angle of 5 °. Separate grains are considered to have high angle grain boundaries and subgrains have low angle grain boundaries. The smallest grain size present was determined independently for each sample, with no grains smaller than 13 pixels in each map. The lowest grain size included was based on whether the initially catalogued smallest grains were truly separate grains or erroneous mis-indexed points. At typically 13 or 14 pixels the smallest grains catalogued by the *HKL* software were considered to be actual grains. Noise reduction and exclusion of unindexed data of the EBSD outputs was conducted following the procedure outlined in Cross et al. (2017). Dauphiné twins were omitted by merging grains separated by misorientations about [001] of 60 ± 5 °. A comparison of the raw EBSD map and the processed map for sample BH7 is shown in Figure 3.5. Figure 3.5.a displays more precisely defined grain boundaries and the removal of unindexed points. Many of the samples contain a secondary phase of mica which remains unindexed by the software. Most of the samples contain mica as secondary phases, which are not indexed. In

the future, indexing of the secondary mica phase could be used to determine the exact volume of mica present in the samples. These micas are the platy grey/black areas visible in Figure 3.5.

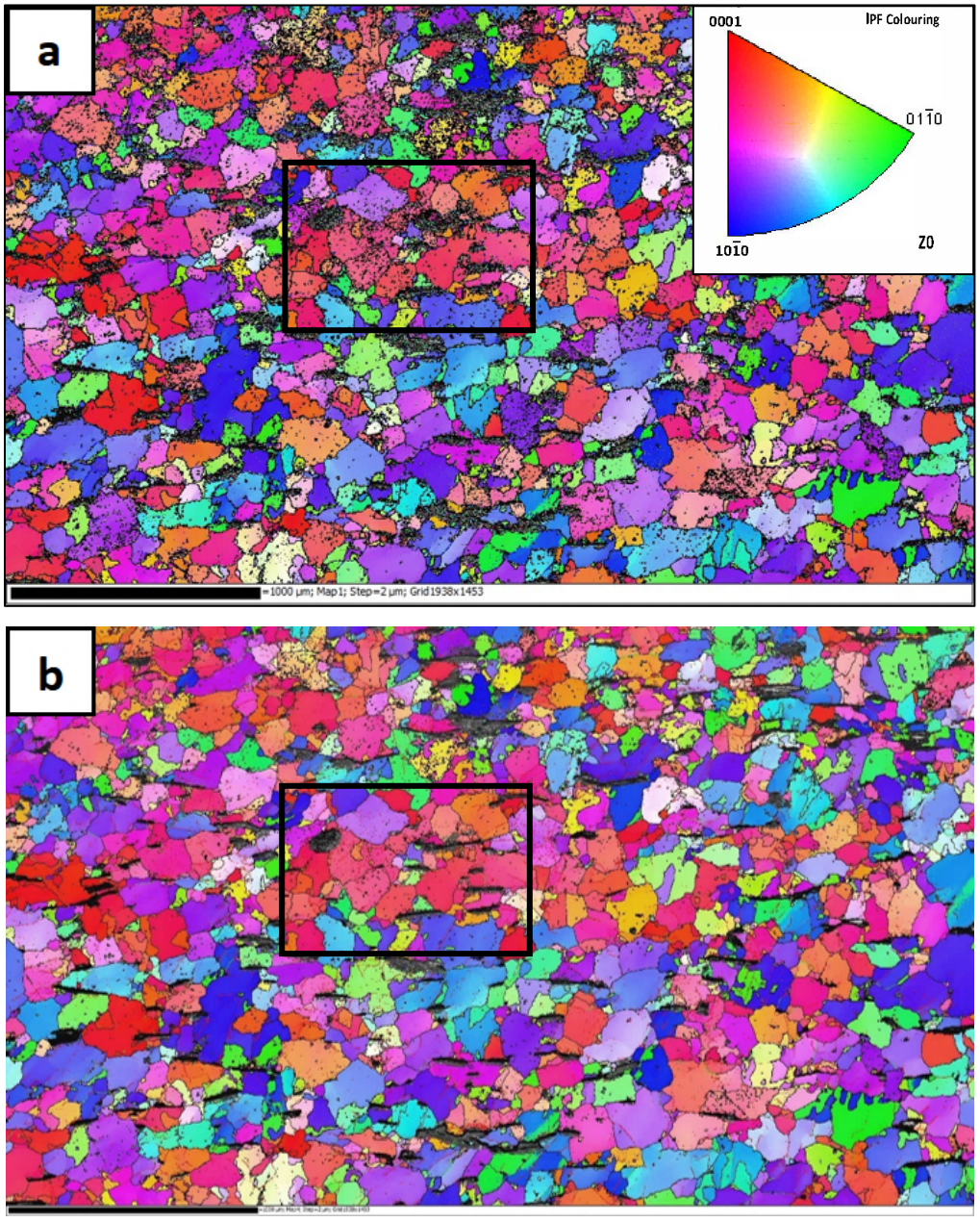

Figure 3.5. Example maps from EBSD analysis with the Inverse Pole Figure (IPF) colouring scheme produced in *HKL Channel 5*. Grains with the same colours are oriented in the same direction. a) The raw orientation grain map of sample BH7 prior to noise reduction. b) The cleaned orientation grain map of sample BH7 post data processing to remove erroneous points. The removal of single pixels and mis-indexed points is most visible in the black box in both images. Red lines in b) outline subgrains. The scale bar is 1000 µm.

3.4 Texture Diagrams

The crystallographic preferred orientation data are presented in upper hemisphere equal area diagrams. Contoured pole figures of the *c, a, m, z* and *r* axes CPOs for each of the detailed runs were produced, using one point per grain of the full dataset. All plots were oriented to align with the macroscopic fabric reference frame, such that the X axis is downdip the lineation and the Y axis is perpendicular to the foliation, the foliation is vertical striking E-W and lineation is horizontal striking E-W. Because the foliation in all outcrops dips approximately to the north and the stretching lineation plunges to the north, all the stereonets were oriented so that the "east" of the diagram is the geographic north. That means the view of all the diagrams is to the west. I also generated CPO pole figures for the subsets of grain populations in each sample. This allows for a comparison between the orientation patterns of the large grains and the small grains in each sample and therefore identification of potential changes of deformation mechanisms. The EBSD data processed in *HKL Channel 5* were also plotted using the open-source MTEX toolbox for MATLAB (https://mtex-toolbox.github.io/). MTEX will be implemented for analysis of the strength and geometry of the CPOs using the Vollmer diagram and the M-index in further research following this study.

Chapter 4: Results

4.1 Microstructural Observations

The quartz mylonites sampled from the Shumar unit of the MCT are composed primarily of quartz with a secondary mineral phase of muscovite present in all samples. The mica grains define the macroscopic foliation and occasionally appear as inclusions in quartz grains. The secondary phase dictates the microstructure in the samples, pinning the quartz grains and limiting growth perpendicular to the foliation. This results in elongated rectangular aggregates of quartz between micas, elongated in the foliation direction and parallel to mica grain boundaries (Figure 4.1). The mica controls the quartz grain size, which is reflected by correlation of modal percentage of mica and the average grain sizes of quartz in each sample (Table 4.1).

There are two dynamic recrystallisation mechanisms present in all samples, grain boundary migration and sub grain rotation recrystallization. No bulging was observed in the quartz microstructure of any mylonite samples. The boundaries between quartz grains are typically curved and interlobate, with window texture, pinning and dragging, indicating grain boundary migration to be the primary mechanism of dynamic recrystallization in the quartzite mylonites (Figure 4.1). The GBM textures are present in the large grains of the samples. Large grains also display partial foam texture (Figure 4.1.f), demonstrated by polygonal grain boundaries and triple junctions at 120 ° (Passchier and Trouw 2005). Foam texture typically forms by grain boundary area reduction during static recrystallisation (Passchier and Trouw 2005). It can also form after a major stress decrease, perhaps by strain softening, or as a steady state dynamic recrystallization microstructure (Kidder et al., 2016, and references therein).

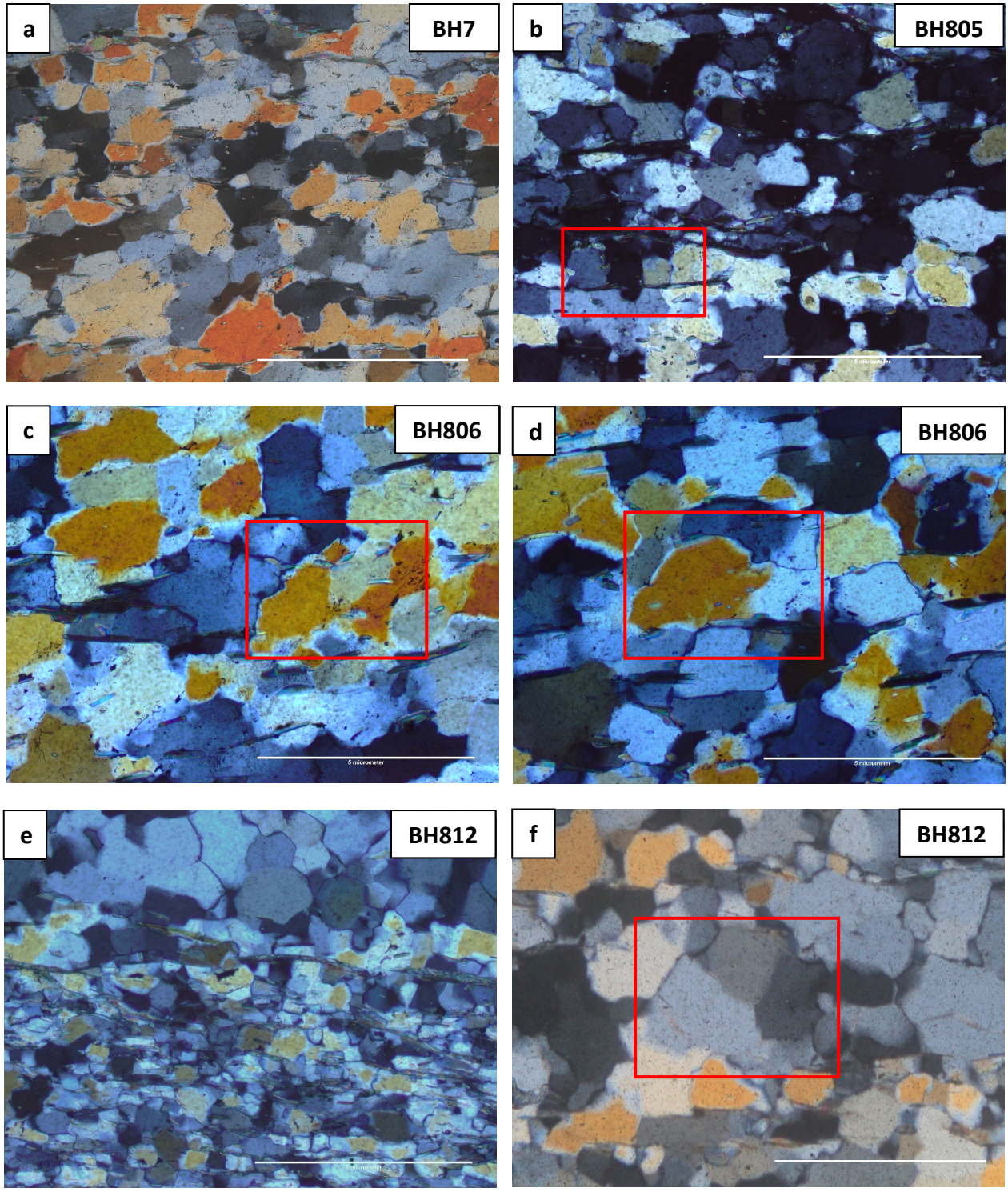

Figure 4.1 Photomicrographs of typical quartz microstructures. (a) Sample BH7 displaying elongation in quartz grains due to a secondary mineral phase. b) Window texture in sample BH805. c) Pinning in sample BH806. d) Dragging of quartz along a muscovite grain in sample BH806. e) Subgrain rotation in sample BH812, f) Sample BH12, illustrating the partial foam texture of the large grains with a triple junction at 120 °. Scale is 500 µm.

Subgrain rotation recrystallization is observed in all of the thin sections. Small grains form from the progressive recrystallization of large grains. Therefore, the large grains are considered relict grains. The small recrystallized grains appear along rims of larger grains (i.e. Figure 2.7.b). The smaller grains do not show undulose extinction or interlobate grain boundaries and are equigranular.

4.2 Grain Size Distribution

We used the *HKL* software to produce grain size measurements of the grains reconstructed from the orientation data. We generated histograms of the grain sizes, using the *DensityPlotter* program (Vermeesch 2012). The observed bimodal distribution of grain sizes indicated the presence of large and small grain populations within each sample. The ratio of large grains to recrystallized grains varies between samples, which is shown by the population density diagrams in Appendix B. We determined the mean grain size of each population based on the population density diagrams (Figure 4.2). We also established the cut-off value separating these grain populations and created subsets of the large and small grain populations in *HKL Channel 5.* The mean grain size diameter for the large and small grain subsets, determined through *HKL Channel 5,* and the associated population density error are shown in Table 4.1. Sample BH809 shows the largest recrystallized grain diameter (13.56 μm) and the smallest relict grain diameter (51.07 μm). Conversely, sample BH1 exhibits the smallest recrystallized grain diameter (9.34 μm) and the largest relict grain diameter (106.98 μm). The mean grain size of the populations within each sample in relation to the percentage of quartz present is displayed in Figure 4.3.

Table 4.1. Mean grain diameter for the large and small grain populations per sample.

Sample	Distance from the MCT (m)	Total No. of Grains Indexed	Small Grain Mean d (µm)	Small Grain d Error*	Large Grain Mean d (µm)	Large Grain d Error*	% Quartz
7	25	1509	12.77	0.035	81	0.33	90
1	100	397	9.34	0.087	107	0.59	95
805	660	878	12.08	0.06	76	0.17	90
806	1512	316	9.78	0.066	74	0.31	85
809	2552	4021	13.56	0.028	51	0.14	80
812	3098	996	11.38	0.069	85.45	0.44	85

* Measurement errors in small and large mean grain diameter are determined through *DensityPlotter*

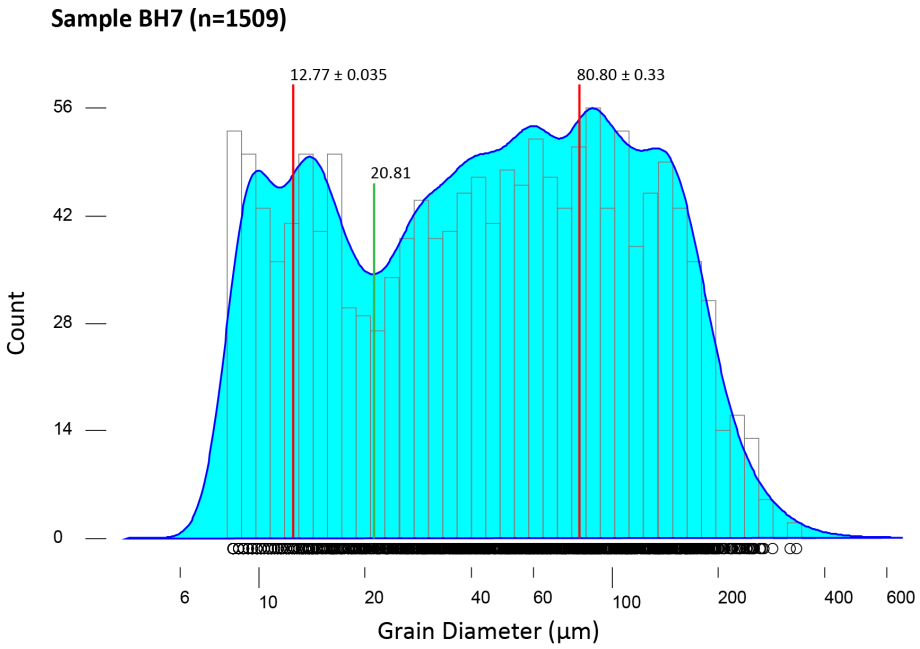

Figure 4.2. The annotated grain size density plot of sample BH7 modified from the *DensityPlotter* software. The small grain population has a mean grain size of 12.77 ± 0.035 µm, large grains have a mean grain size of 80.80 ± 0.33 µm. The cut-off value between the two populations is marked by the green line.

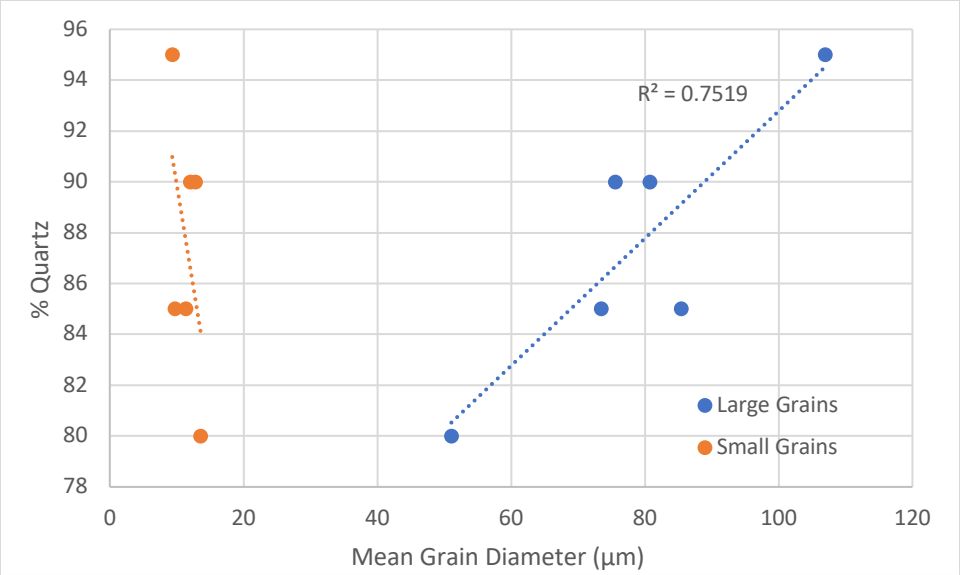

Figure 4.3. The mean grain size of the large and small grain populations and the corresponding modal percentage of quartz in each sample.

4.3 Crystallographic Preferred Orientation Results

All grain maps produced from EBSD orientation analysis are included in Appendix A. The corresponding contour pole figures created from the orientation data are also presented in Appendix A, including those created from the separated large and small grain subsets. The CPO pole figures generated using one point per grain from the full dataset for each sample are shown in Figure 4.4. The X-axis is parallel to the lineation and the Y-axis is perpendicular to the foliation.

BH7

The *c*-axis pole figure for sample BH7 shows a broad partial Type I girdle of Lister (1977), with a strong northern rhomb maximum and a second much weaker rhomb maximum in the south. The *a*-direction pole figure displays a corresponding great circle perpendicular to the main *c*-axis maximum, with one weak basal maximum on the periphery. A weak great circle perpendicular to the northern *c*-axis maximum is also exhibited in the *m*-axis distribution. The *r*- and *z*- axes appear to be distributed along a small circle around the *c*-axis maximum.

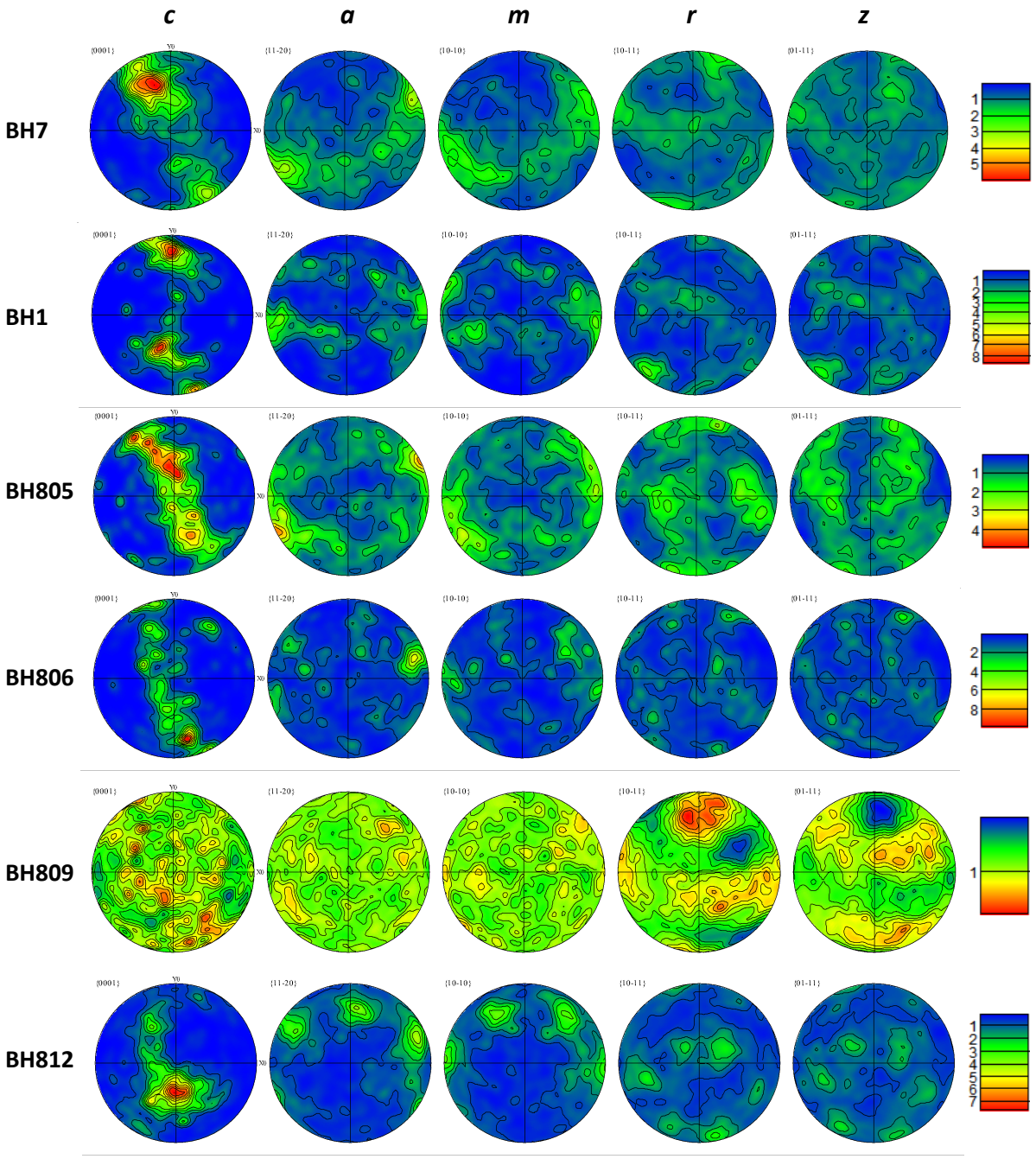

Figure 4.4. The crystallographic preferred orientation pole figures of the full dataset of each sample, generated using one point per grain. Pole figures are plotted for the *c, a, m, r* and *z* axes of quartz. Samples are ordered with increasing structural distance from the MCT. All the plots are oriented so that the macroscopic foliation is vertical, striking E-W and the macroscopic lineation is horizontal, striking E-W and plunging to the E. Because in nature the foliation is shallowly north dipping and stretching lineation shallowly north plunging, the "view direction" of all diagrams is to the west.

BH1

Poles of the *c*-axis are distributed along a partial, asymmetric Type I cross girdle. There are two rhomb maxima of similar strength in the *c*-axis with a third, weaker basal maximum on the southern periphery. A very weak basal maximum is present along the periphery of the CPO in the *a*-direction. The CPOs for the other axes show no visible pattern.

BH805

The *c*-axis shows a distinct partial, asymmetric Type I girdle with northern rhomb and basal maxima. The *a*-direction displays a weak maximum in the periphery perpendicular to the *c*-axis girdle with all the poles suggesting a weak small circle with a large opening angle. There are is also a weak *m*-axis maximum in the periphery. A broad small circle with three maxima about the X-axis and perpendicular to the dominant *c*-axis maximum is present in the CPO of the *z*-axis.

BH806

The *c*-axis CPO exhibits a weak partial Type I girdle, similar to BH805. Counter to the previous samples, the strongest maximum of c- axis is located on the southern periphery. This *a*-direction has one maximum on the periphery perpendicular to the *c*-axis girdle and a faint distribution along a small circle with large opening angle and c entered around the Z-axis. The *r*-axis and *z*-axis show similar weak small circles perpendicular to the *c*-axis maximum.

BH809

Sample BH809 has a much weaker CPO than the other mylonites. However, multiple maxima are concentrated along a great circle suggesting a partial Type I cross girdle pattern. The *r*-axis yields a stronger pattern with a maximum near the periphery of the Y-axis. The *z*-axis displays a weak small circle about the Y-axis in the north and south of the diagram. This is contradictory to the expected patterns in the *r*-axis and *z*-axis of three maxima forming a small circle perpendicular to the *c*-axis maximum which is displayed by sample BH12. The apparent trend displayed by the *r* and *z* axes suggests the CPO requires rotation to align with the microscopic foliation.

BH12

The BH12 CPO is the clearest pattern with highest densities, displaying an ideal quartz preferred orientation pole figure. The *c*-axis CPO is characterized by a strong southern rhomb maximum and a partial, asymmetric partial Type I cross girdle. There are three *a*-direction maxima along a great circle, perpendicular to the rhomb maximum of the *c*-axis. The strongest of the three *a*-direction maxima is nearest the X-axis. A similar pattern is shown in the *m*-axis CPO with the three maxima located between the *a*-direction maxima. The three maxima of both the *r*- and *z*- axes are visible, creating a small circle centred around the *c*-axis maximum.

Separation of the large and small grain CPOs typically results in large grain subsets CPOs that present the same pattern as the full datasets with stronger densities. This is demonstrated most clearly by samples BH7, BH805 and BH806 (Figure 4.5). The small grain CPOs of these samples primarily present weaker but similar CPO patterns from those displayed in the large grain and full dataset pole figures.

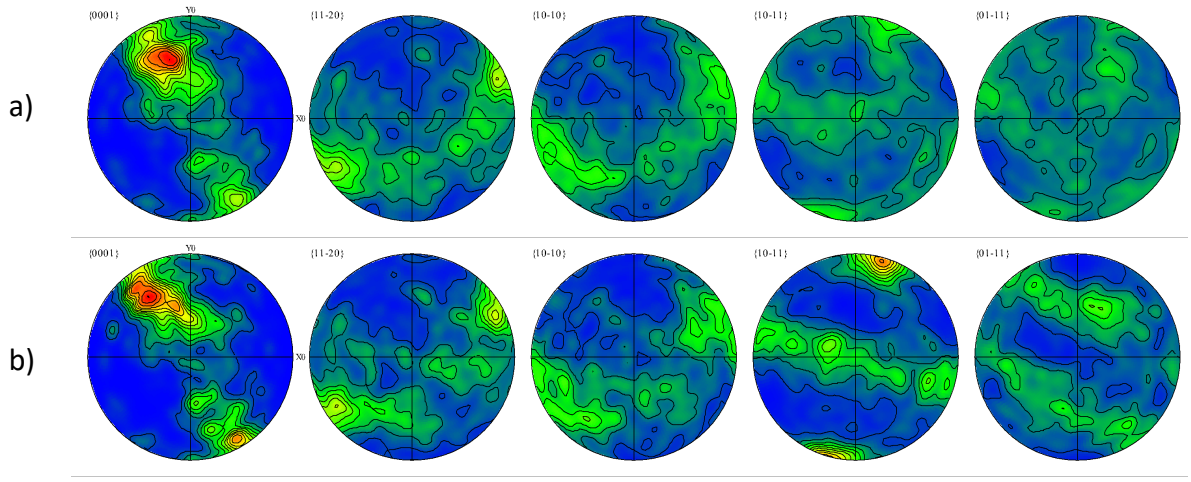

Figure 4.5. Grain size effect on the CPO. a) The full dataset pole figures of sample BH7 and b) the corresponding large grain subset pole figures, which display stronger maxima densities but the same CPO patterns for the *c-, a-* and *m*-axes.

Chapter 5: Discussion

5. 1 Dynamic Recrystallization Mechanisms

The microstructures and bimodal grain distribution present in the samples of MCT mylonites reveals a two-stage deformation history. The large grain populations display grain boundary migration, forming at higher temperatures and lower stresses. These large grains are interpreted to be relict grains of the peak-temperature stage of deformation. The small grain populations are interpreted to reflect a second stage of deformation by sub grain rotation recrystallization as the rocks were exhumed and subjected to greater stresses at lower temperatures. Subgrains and the recrystallized grains partially overprint the GBM texture. The presence of SGR and GBM in the quartzite mylonites also provides an estimate of deformation temperatures between ~400 °C and ~550 °C (Stipp et al. 2002). The presence of partial foam texture in the relict grains of the MCT samples indicates that the larger grains did not reach equilibrium before stresses increased, as many of the grains do not show the characteristic polygonal boundaries and triple junctions at 120 ° (Kidder et al. 2016). Grain sizes from a partial foam texture impose a lower limit on the flow stresses of the earlier stage of deformation.

5.2 Grain Size Distribution Analysis

Samples with a higher modal percentage of quartz show a larger grain size for the large relict grain populations, as displayed by sample BH1 (Table 4.1). Grain size correlates to the limiting effect secondary phases have on the growth of quartz grains. The relationship between grain size and the percentage of quartz in each sample is shown in Figure 4.3. Sample BH809, which exhibits the smallest large grain size population, has the lowest percentage of quartz (80%). A much higher number of quartz grains (4021) were indexed in sample BH809 in comparison to the other samples. This indicates that there is a greater proportion of recrystallized to relict grains in BH809. This sample also shows greater amounts of pinning and dragging as a result of the higher proportion of mica. The BH809 CPO is likely an outlier due to the high proportion of small grains to large grains, as well as the lower percentage of quartz present.

5.3 Dominant Slip Mechanisms and Strain Geometry

The locations of the orientation maxima in the *c*-axis and *a*- direction of the full dataset CPOs indicate that the dominant slip system in the MCT quartz mylonites is rhomb <a> (Bouchez 1978, Schmid and Casey 1986). The quartz fabric in the large grains primarily presents the same pattern and slip system as the full dataset. CPOs of the small grain subsets present weaker patterns than the large grain subsets. Yet, they reflect the trend of Type I cross girdles in the *c*-axis. Maxima often appear closer to the centre of the *c*-axis CPO in the small grain subsets, suggesting a potential transition to prism <a> slip during the second stage of deformation. EBSD orientation analysis focusing specifically on domains with high level of SGR recrystallization within these samples and closer to the core of the MCT mylonitic belt would be required to confirm this trend.

All of the samples display partial Type I cross girdles (Lister 1977) in the *c*-axis CPOs. Type I cross girdles that develop as a result of plane strain are much more common than Type II girdles, which develop in constrictional settings (Schmid and Casey, 1986; Passchier and Trouw, 2005). Trends in the *a*-direction CPOs are less clearly defined; however, maxima are predominantly present along the periphery most often forming a great circle perpendicular to the strongest maximum of the *c*-axis. The only maxima located closer to the centre in the *a*-direction CPO are in sample BH812. The quartz CPO in the *a*-direction presents large opening angles which also indicates dominance of non-coaxial plane strain.

5.4 Stress Profile Across the MCT

5.4.1 Flow Stresses and Quartz Flow Laws

The sliding resolution grain size paleo piezometer for quartz from Cross et al. (2017) was utilized to calculate the flow stresses for the relict and recrystallized grains. This piezometer is the first EBSD based recrystallized grain piezometer established using internal distortion to separate relict and recrystallized grains. The piezometer relationship was calibrated as:

$$D=10^{4.22 \pm 0.51} \cdot \sigma^{-1.59 \pm 0.26} \quad (2)$$

where D is the mean diameter of the grain populations and σ is differential stress (Cross et al. 2017). We employed the sliding resolution piezometer as it focuses specifically on estimating the stresses in fine-grained (<10 μm) samples, combining 1 μm step size data at larger grain sizes with 200 nm step size data at finer grain sizes.

The rearranged piezometer relationship, $\sigma = \left(\frac{D}{10^{\gamma}}\right)^{1/n}$, contains three parameters with associated error, γ, D and n. The measurement error (δ_D) in grain size (D) is determined through the *DensityPlotter* program (Table 4.1). The uncertainty values associated with γ and *n* ($\delta_\gamma = \pm 0.51$ and $\delta_n = \pm 0.26$) were determined by best fit relationships calculated by Cross and co-workers (2017). To calculate the error associated with the calculated differential stress one has to propagate the error from these parameters through the piezometer equation. Upon rearranging the standard uncertainty relationship and factoring the partial derivatives the equation becomes:

$$\delta\sigma = \frac{\sigma}{n}\sqrt{\frac{{\delta_D}^2}{D^2} + \log^2(10)\,{\delta_\gamma}^2 + \log^2(\sigma)\,{\delta_n}^2} \qquad (3)$$

The uncertainty values corresponding to the calculated flow stresses are shown in table 5.1. The uncertainty associated with the flow stresses of the small grains calculated from equation 3 is currently large, which is expected based on the formula for error propagation in which largest error is derived from the smallest grain size. This must be refined in future work and will be discussed further in Chapter 6.2.

Table 5.1. Differential stress and calculated uncertainty for the large and small grain sizes.

Sample Number	Differential Stress of Small Grains (σ, MPa)	δσ (Small Grains)	Differential Stress of Large Grains (σ, MPa)	δσ (Large Grains)
7	90.86	41.18	28.47	11.37
1	110.6	51.24	23.87	9.356
805	94.09	42.81	29.69	11.91
806	107.5	49.62	30.22	12.14
809	87.49	39.49	38.00	15.65
812	97.69	44.64	27.49	10.94

To constrain the strain rates of the mylonites we employed the quartz dislocation creep flow law formulated by Hirth et al. (2001). This law is expressed as:

$$\dot{e} = A f_{H_2O}^{m} \sigma^{n} \exp\left(\frac{-Q}{RT}\right) \quad (4)$$

Where $\dot{e}$ is strain rate, A is a material parameter, f_{H_2O} is the fugacity of water, m is the water fugacity exponent (≈1), σ is the differential stress, n is the stress exponent for quartz, Q is the activation energy, R is the gas constant (8.314) and T is the absolute temperature. Hirth et al. (2001), analytically determined the values of log$A$ = -11.2 ± 0.6 MPa^{-n}/s and Q= 135kJ/mol, assuming *m*=1 and *n*=4. Tokle et al. (2019) demonstrated the stress exponent for quartz (n) is not constant. Accordingly, the stress exponent of *n*=4 was employed for the large grains, which underwent deformation at higher temperatures and lower stresses, and *n*=3 was used for the small grains, which formed at lower temperatures and higher stresses. The difference in stress exponents also corresponds to a transition in the dominant slip system. By analysis of experimental data Tokle et al. (2019) determined slip on the prism <a> system to dominate at low stresses, whereas at higher stresses slip on the basal <a> is indicated. At higher temperatures and low stresses, we observe maxima corresponding to rhomb <a> slip in the MCT quartz fabric, and at lower temperature and higher stresses (during the second stage of deformation) *c*-axis maxima migrate towards the centre of the CPO pole figures, forming a Y-maximum of the *c*-axis, suggesting prism <a> slip.

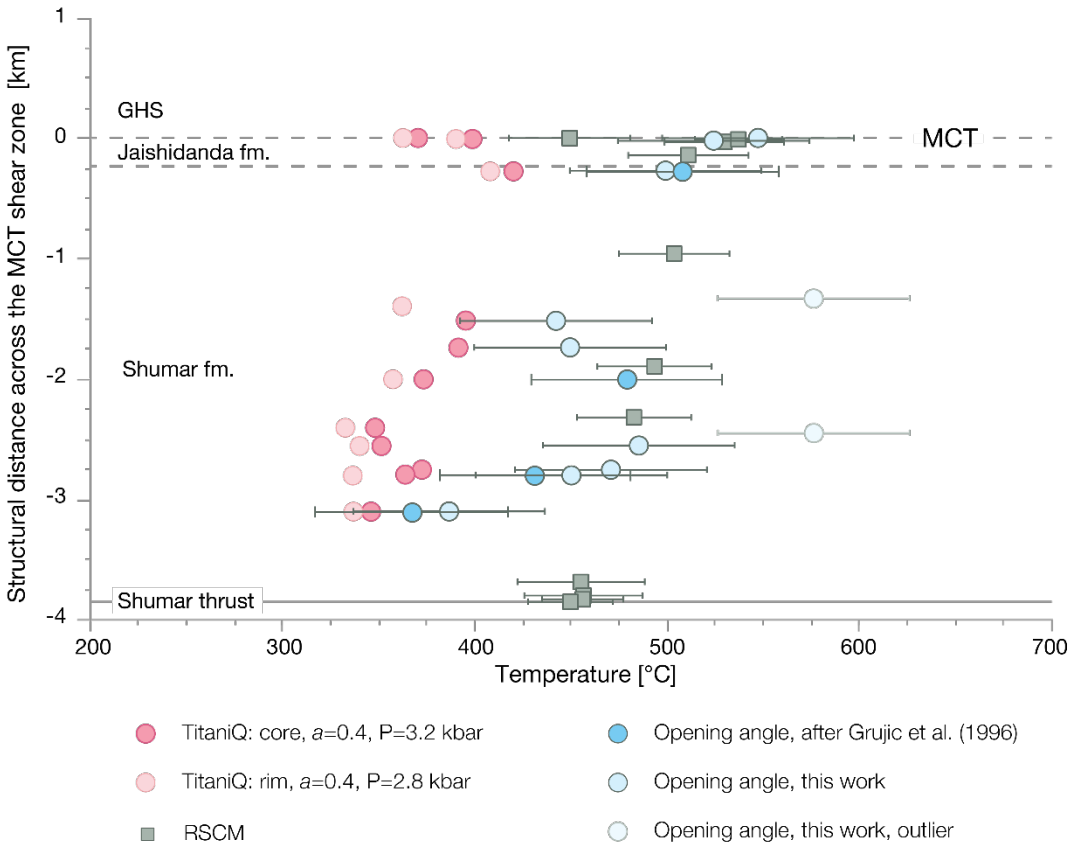

Figure 5.1. Deformation and metamorphic temperatures through the LHS in eastern Bhutan plotted with increasing structural distance from the MCT (Grujic et al. 2020). The temperatures of deformation decrease with increasing distance from the MCT.

Deformation temperatures were determined independently by Grujic et al. (2020) using three different methods, Raman spectroscopy of carbonaceous material for the peak metamorphic temperature, the opening angle of the *c*-axis in quartz CPO diagrams, and titanium in quartz (TitaniQ) thermobarometry (Figure 5.1) for the deformation temperature. They concluded that the opening angle temperatures correspond to the minimum temperature of the earlier (at peak metamorphic temperature) stage of deformation associated with the large grains, from coincidence of the RSCM and opening angle temperatures. The TitaniQ rim values represent estimates of the minimum conditions (Figure 5.1) of the second stage of deformation producing the small recrystallized grains. Temperatures calculated by all three methods decrease with increasing structural distance from the MCT, i.e., with increasing depth, which defines an inverted temperature gradient across the thrust zone.

Pressures used to calculate fugacity were determined by Grujic et al. (2020) through modelling of multiple thermochronological datasets. Calculated temperatures were refined with iterative calculations; meaning an initially calculated temperature was used to estimate the depth, and therefore pressure, at which an individual model particle path crossed the target temperature range. That pressure was inserted into the temperature calculation equation which resulted in a more accurate temperature. The process was repeated until the guess temperature equalled the calculated temperature. The applied method yielded temperatures between 337 ± 50 °C and 400 ± 50 °C for the small grains and between 387 ± 50 °C and 400 ± 50 °C for the large grains. The water fugacity values for both peak and retrograde deformation conditions were determined from these constrained temperatures and pressures using the fugacity calculator by Withers (https://www.esci.umn.edu/people/researchers/withe012/fugacity.htm). The estimated temperature, pressure and fugacity values are shown in Appendix C.

From the calculated variables a complete flow stress profile was produced (Figure 5.2). The quartz dislocation creep flow law of Hirth et al. (2001) yields estimates of strain rate between 5.0 x 10^{-16} s^{-1} to 1.4 x 10^{-14} s^{-1} for the small grains, and strain rates from 4.0 x 10^{-15} to 2.1 x 10^{-12} s^{-1} for the large grains. The flow stresses (σ) are plotted against temperature in Figure 5.1, along with the strain rate curves of Hirth et al. (2001) and Rutter and Brodie (2004). The flow law by Hirth et al. (2001), yields reasonable strain rates whereas the flow law of Rutter and Brodie (2004) does not fit the data, underestimating the strain rates (Figure 5.2).

To the best of my knowledge the flow stress profile was only once before applied in a collisional regime by Law et al. (2013) in the western Himalaya. They produced a strength profile from the hanging wall block of the Main Central Thrust (the GHS). Quartz mylonites from the MCT core and up to 1 km above the MCT yielded strain rates of 10^{-14} s^{-1} to 10^{-11} s^{-1}. The strain rates display a structural trend of increasing from the rim downwards to the core of the shear zone. They calculated flow stresses between 7 and 30 MPa, which increase from the rim to the core of the shear zone (Law et al. 2013). Strain rates between 10^{-15} s^{-1} to 10^{-12} s^{-1} from our MCT footwall samples are consistent with the strain rates in the hanging wall block of the MCT derived by Law et al. (2013) from the GHS mylonites.

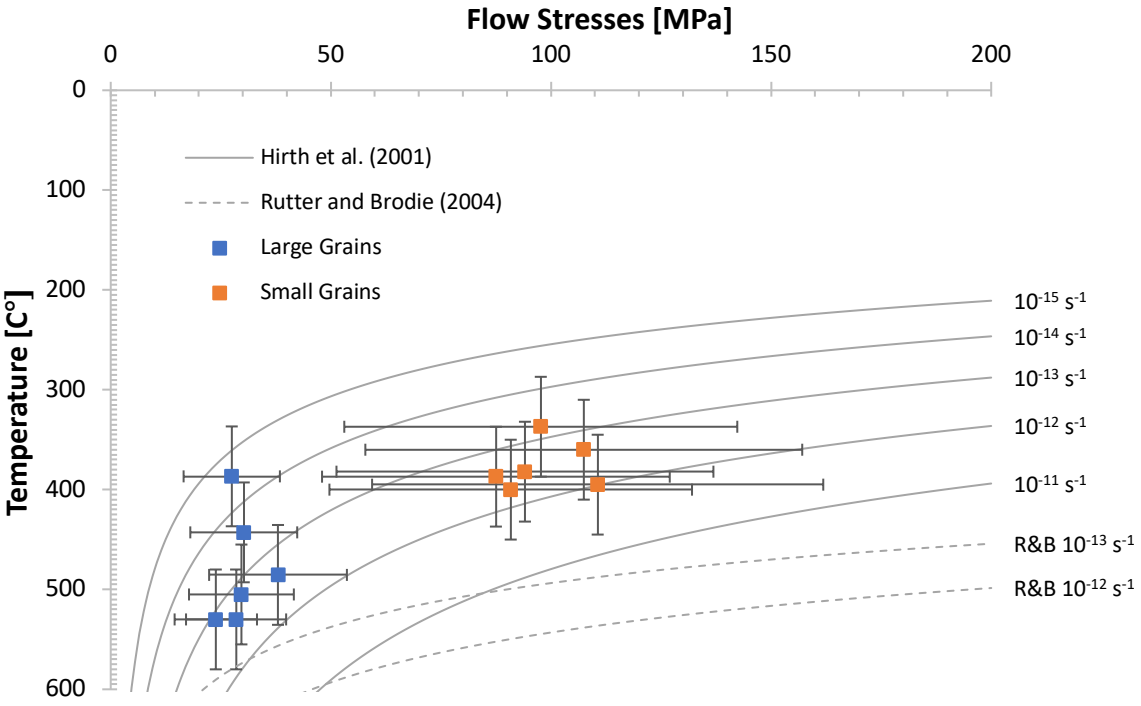

Figure 5.2. Flow stresses of the large grains (blue) and small grains (orange). The error bars of individual data points represent uncertainties in temperature, grain size and the error associated with the paleopiezometer of Cross et al. (2017). The flow law of Hirth et al. (2001), plotted with solid lines, borders the data of both populations between 10^{-15} s^{-1} to 10^{-12} s^{-1}. The strain rate curves according to Rutter and Brodie (2004), are unreasonably slow for a shear zone.

Large grains from my study area show little variation in flow stresses ranging from 26 to 30 MPa. However, strain rates vary greatly with structural distance and temperature from the rim to the core of the shear zone. The deformation temperatures of large relict grains range from 386.7 ± 50 °C to 530.0 ± 50 °C and the strain rates from 10^{-15} s^{-1} to 10^{-12} s^{-1} . The inverted temperature gradient is also demonstrated by the trends of *c*-axis patterns in the CPO pole figures and the independently constrained temperatures by Grujic et al. (2020). The finer recrystallized grains yield a range in flow stresses from 87 MPa to 110 MPa at temperatures from rim to core, between 337.0 ± 50 °C and 400.0 ± 50 °C. We conclude that the stresses calculated from the small recrystallized grains correspond to deformation at the base of the brittle ductile transition zone as these are the maximum flow stresses observed in the samples.

Therefore, the maximum differential stress of ~110 MPa in the ductile regime is determined to approximate the peak stresses of the shear zone. Through thermal modelling Grujic et al. (2020) constrained the depth of the MHT at transition temperature range to about 11 km (Figure 5.6).

5.4.2 Brittle Stress Envelope

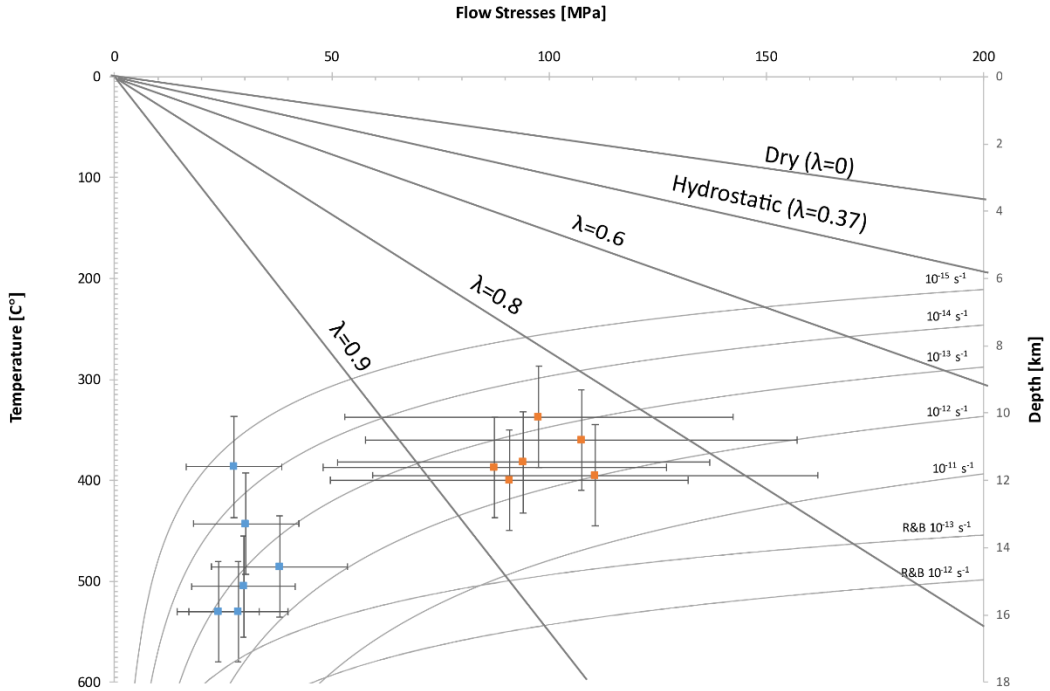

Figure 5.3. The extrapolation of Byerlee's Law for various pore fluid pressures (λ= 0, 0.37, 0.6 0.8, 0.9). The maximum stress of the small grain approximates the peak stresses along the MCT and the transition from ductile flow stresses to linear brittle differential stresses must occur near this point.

Byerlee's Law models critical shear stress through the frictional upper crust. It relates the shear stress required for faulting on a fracture and the normal stress across it, with the normal stress associated with the depth through the crust. The extrapolation of Byerlee's Law is shown in Figure 5.3 for various pore fluid pressures. The Brittle stress curve for a hydrostatic pore fluid pressure (λ= 0.4) does not transect the calculated flow stresses of the ductile regime. A stress profile through the brittle and ductile regimes of the MCT requires a greater pore fluid pressure of approximately λ=0.85. Mallyon (2014) determined through analysis of the critical taper angle of the Himalayan orogenic wedge that values of pore fluid pressure between λ= 0.8

and λ= 0.95 are acceptable for the MCT. The conditions constrained by the stress profile have implications for the Himalayan Megathrust, along which the rocks of the MCT footwall were ductilely deformed. With the MHT dipping at 12° (Grujic et al. 2020) the constructed Mohr circle diagram for the maximum differential stress (110 MPa) at ~11 km depth indicates that a pore fluid pressure of approximately λ= 0.85 (~247 MPa) is required for continued slip along the MHT (Figure 5.4, Figure 5.5). The Mohr circle is constructed under the assumption that the maximum principal stress ($\sigma_1 = \sigma_3$ + 110 MPa) is horizontal, and vertical principal stress is $\sigma_3 = \rho gh$. Through geophysical observations it was determined that the coefficient of friction along the MHT is μ= 0.4 (Hammer et al. 2013, Grujic et al. 2018), rather than 0.85. the pore fluid pressure required for sliding is approximately 246.50 MPa, corresponding to λ= 0.846.

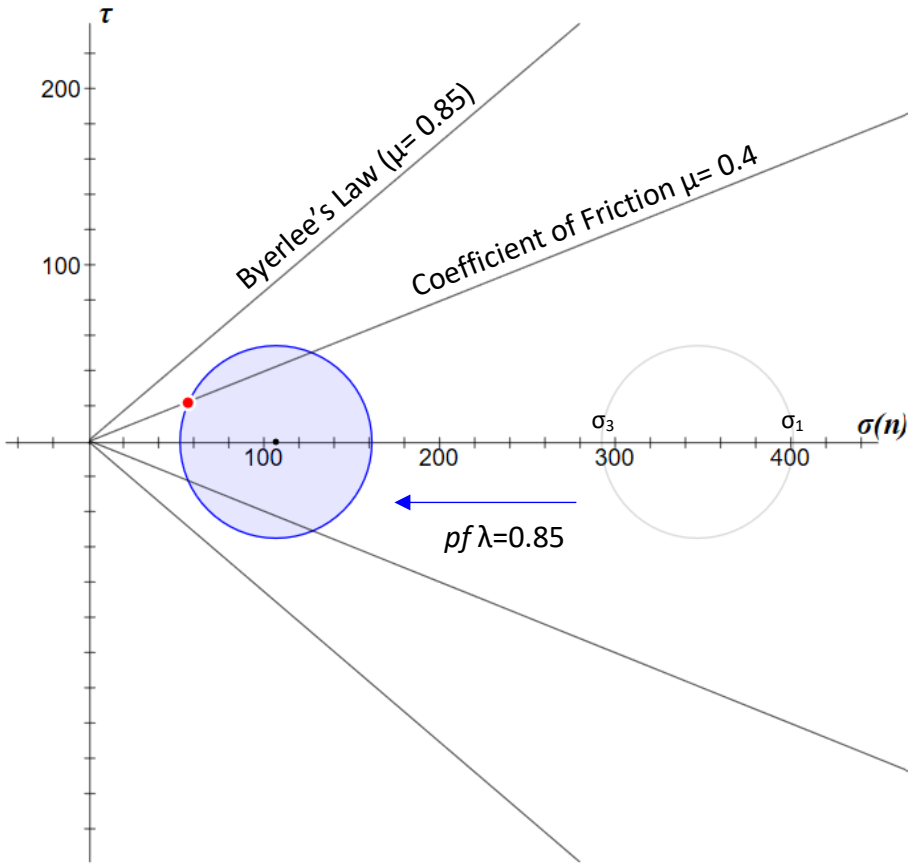

Figure 5.4. The Mohr circle constructed for the estimated maximum differential stress of ~110 MPa at 11 km depth with the surface stresses along the MCT plane dipping 12 ° (θ=78 °) plotted in red. σ_1= 401.357 MPa and σ_3 = 291.357 MPa. Therefore, a λ~0.85 and coefficient of friction of 0.4 is required for frictional slip along the MHT in the seismogenic zone.

5.5 Stress Profile Analysis

Merging the appropriate brittle stress envelope with flow stresses of the ductile regime produces the completed stress profile of the MCT shown in Figure 5.6. The profile illustrates the strength of the crust through the BDT, with a maximum stress of ~110 MPa at 11 km depth. In theory, this profile can be used as a proxy for the strength of deforming rocks at different depths in a crust. However, the geothermal gradient varies across the MCT due to the overthrusting of hot GHS rocks over colder LHS rocks (Figure 5.5).

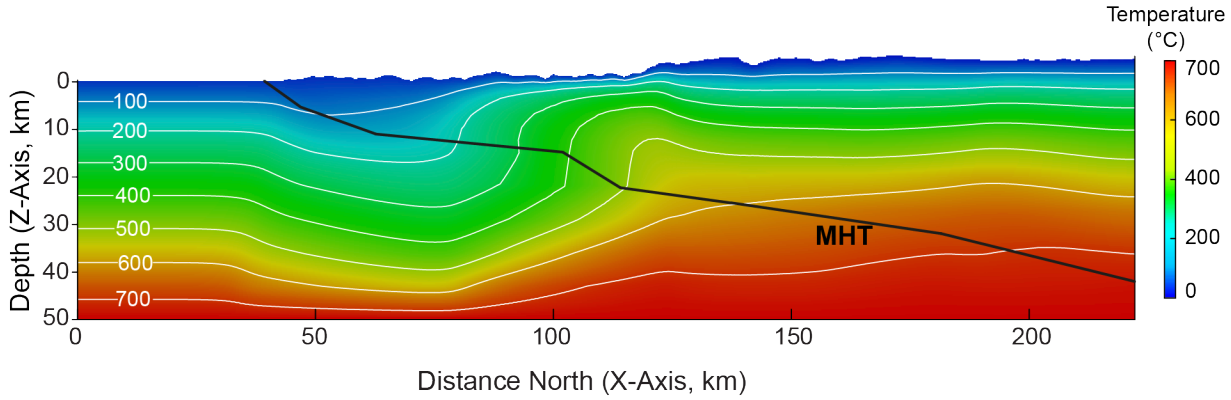

Figure 5.5. The solution to thermo-kinematic modelling for the geometry of the MHT. Isotherms, shown in white, display the significant perturbations present in the subsurface thermal field of the Himalayan orogen. From Grujic et al. (2020).

Locally this can form an inverted temperature gradient as observed across the LHS and the MCT zone in Bhutan and elsewhere in the Himalaya (Grujic et al., 2020, and references therein). For this reason, the peak deformation temperature decreases across the MCT shear zone, from the core towards the margin, about 3 km deeper. This results in estimated strain rates that range from the fastest in the core, 2.1×10^{-12} s^{-1}, to slowest at the shear zone margins, 4.0×10^{-15} s^{-1}. The stress profile illustrates that decreasing strain rate is more effective at lowering differential stress than decreasing temperature. Therefore, with these variable strain rates and temperature gradients, the generated strength profile is only applicable to the MCT shear zone, not to the encompassing continental crust. The stresses calculated from the large and small grain populations were also not effective coevally. From this we conclude that

the strength profile actually represents a stress history of the MCT, providing a snapshot of differential stresses through time and along the shear zone.

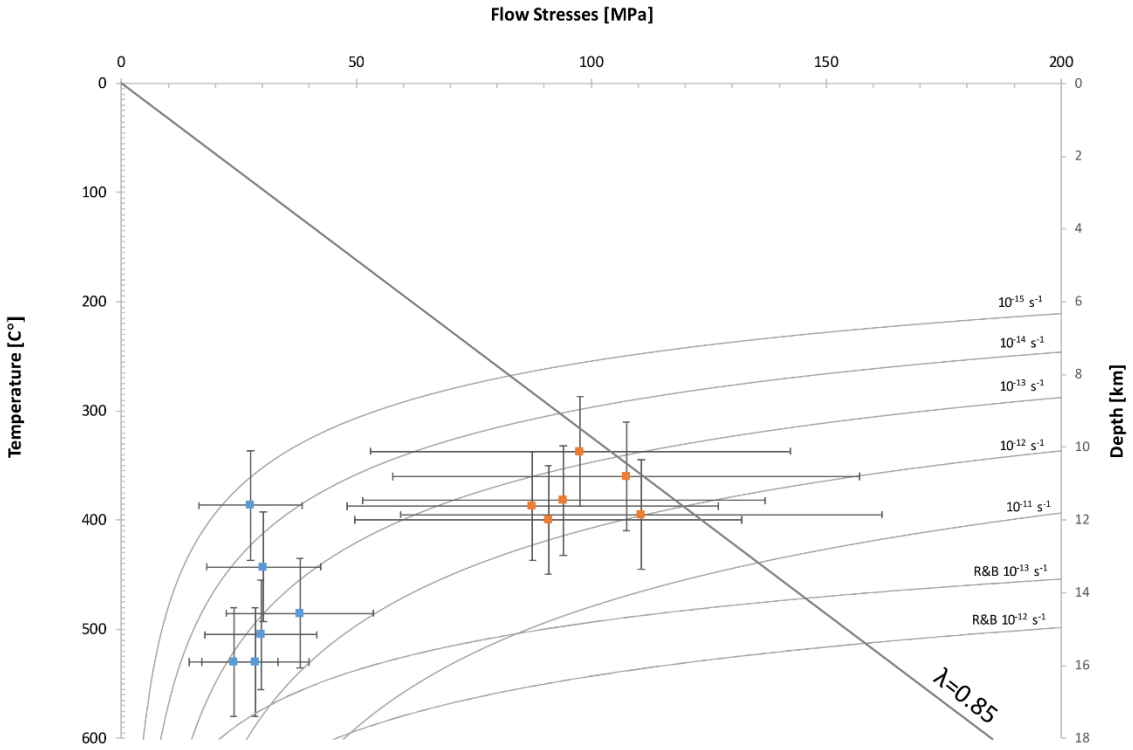

Figure 5.6. Strength profile in temperature-σ space of the Main Central Thrust shear zone. For the large grains (blue symbols) the highest deformation temperatures were recorded in the core of the shear zone and the lowest deformation temperatures at the shear zone margin, 3 km deeper, which corresponds to Figure 5.1. Large and small grain populations formed in succession and therefore the strength profile represents an evolution of stress through time along the shear zone.

The stress profile through the brittle and ductile regimes of the MCT indicates that the Main Himalayan Thrust is weak, with a low coefficient of friction (μ=0.4) and high pore fluid pressure (λ=0.85). Nevertheless, this thrust is still able to produce mega earthquakes, such as the magnitude 8.2 earthquake of 1714 in Bhutan that ruptured the surface of the MFT (Hetényi et al. 2016).

Chapter 6: Conclusion and Recommendations for Further Research

6.1 Conclusion

The exhumed footwall of the Main Central Thrust in eastern Bhutan provides a unique opportunity to observe rocks deformed in the ductile regime of the Main Himalayan Thrust. The exposed rocks preserve a record of their stress evolution through the ductile and brittle regimes of the crust. We examined quartzite mylonite samples from two transects through the Shumar Unit of the Lesser Himalayan Sequence. Microstructural and quartz CPO fabric data obtained through EBSD analysis reveal a bimodal grain size distribution with two grain size populations that reflect a two-stage deformational history. Large relict grains exhibit grain boundary migration, with the minimum temperatures of deformation between 386.7 $\pm$ 50 °C and 530.0 $\pm$ 50 °C. Small recrystallized grains formed by sub grain rotation recrystallization at temperatures between 337. 0$\pm$ 50 °C and 400.0 $\pm$ 50 °C. Quartz CPOs in the *c*-axis display type I cross girdles, indicating deformation by plane strain. This is reinforced by the large opening angles present in the *a*-direction CPOs which suggest noncoaxial plane strain to flattening strain. We surmise that the dominant slip system is rhomb <a> from the locations of the maxima present in the large grain population and full dataset CPOs.

We constructed a stress profile of the brittle upper crust and ductile middle segment of the MCT through grain size analysis integrated with temperatures and pressures of deformation. Flow stresses of the relict grains range from 26 MPa to 30 MPa. Small grains show a greater variation in flow stresses from 87 MPa to 110 MPa. From the strength profile it is determined that the maximum differential stress of the MCT is approximately 110 MPa. The peak stresses correspond to the base of the brittle ductile transition zone, which is determined to reside at ~11 km depth. Application of the quartzite flow law of Hirth et al. (2001) yields strain rates from 4.0 x 10^{-15} to 2.1 x 10^{-12} for the large grains and strain rates of 5.0 x 10^{-16} s^{-1} to 1.4 x 10^{-14} s^{-1} for the small grains. The quartzite flow law of Rutter and Brodie (2004) estimates unreasonably slow strain rates for a shear zone.

The initial intent of this study was to produce a strength profile of the Himalayan crust. However, the MCT displays an inverted temperature gradient and variable strain rates from

core to rim. Therefore, we conclude that the profile is not applicable to the surrounding crust. As the grain populations that record the stages of deformation conditions were not effective coevally, we also conclude that the profile constructed represents a stress evolution through time along the shear zone. The microstructural observations, quartz CPOs and stress profile provide insight to the ductile deformation occurring at depth along the MHT. This maximum differential stress (110 MPa) is consistent with the conditions required for continued slip along the Main Himalayan Thrust, with a coefficient of friction of $\mu = 0.4$ and a pore fluid pressure of $\lambda = \sim 0.85$. The conditions for continued slip suggest that the MHT is weak but still capable of mega earthquakes.

6.2 Recommendations for Further Research

There are several opportunities for expansion on this project, which will improve the constraints of the constructed stress profile and the history it represents, as well as the conditions of deformation through the MCT. We acknowledge that uncertainties associated with the profile are currently large, however future work towards establishing the P-T-T history through methods such as microstructural analysis will enhance its accuracy and precision. Several approaches for further research include:

1. *EBSD Analysis*. Six samples were mapped at the 2 μm step size for this study. EBSD analysis should be performed for more mylonite samples along the 3 km transects. This will increase the accuracy of the mean grain sizes recorded, as well as allow for increased observations of trends present in the quartz microstructure and CPO. An increase in sample size will also contribute to decreasing the error calculated from equation 3, as the standard error will be significantly smaller. We also suggest indexing the mica phase to compare the percent volume of the secondary phase to quartz in the samples. This could also be conducted with feldspar which is present in the Jaishidanda Formation. Furthermore, production and examination of the CPO inverse pole figures will provide a more holistic representation of the dominant slip systems present through the deformational history.

2. *Quantifying the Strength of the CPOs.* The strength and geometry of the CPO can be quantified through a Vollmer diagram, which displays the *P, G* and *R* indices of the *c*-axis distribution (Vollmer 1990, Barth et al. 2010). The indices represent how strongly the data define a point (*P*), girdle (*G*) or random *(R*) distribution. The fabric intensity can also be calculated in MATLAB by the M-index which compares the expected distribution of misorientation angles in a completely random fabric to the distribution of misorientation angles between grains in a sample (Skemer et al. 2005, Starnes et al. 2020). The relationship between CPO patterns and strain magnitude is clearly defined (e.g. Heilbronner and Tullis 2006). Therefore, measurement of the strength of the CPO through these parameters will further delineate relative strain patterns and the variations in strain magnitude through the footwall of the MCT.

3. *Grain Population Separation.* The current method of separating grain populations with a grain size threshold is required to create subsets of grain populations in *HKL Channel 5* for CPO analysis. However, this method might skew differential stress estimates as it is not able to fully separate overlapping grain size distributions (Cross et al. 2017). To obtain a more precise ratio of relict to recrystallized grains a method that isolates these types of grains independently of grain size should also be implemented. The *Recrystallized Fraction Component* in *HKL Channel 5* detects deformed and recrystallized grains in the orientation map by determining if the average angle in a grain exceeds the critical misorientation angle that defines a subgrain classified by the user. Separating the relict and recrystallized grains can also be executed using the MTEX toolbox for MATLAB by quantifying the degree of intracrystalline lattice distortion in each grain (Cross et al. 2017).

References

Avouac, J.P. 2015. Mountain Building: From Earthquakes to Geologic Deformation. *In* Treatise on Geophysics: Second Edition. Elsevier B.V. doi:10.1016/B978-0-444-53802-4.00120-2.

Barth, N.C., Hacker, B.R., Seward, G.G.E., Walsh, E.O., Young, D., and Johnston, S. 2010. Strain within the ultrahigh-pressure Western Gneiss region of Norway recorded by quartz CPOs. Geological Society Special Publication, **335**: 663–685. doi:10.1144/SP335.27.

Behr, W.M., and Platt, J.P. 2011. A naturally constrained stress profile through the middle crust in an extensional terrane. Earth and Planetary Science Letters, **303**: 181–192. doi:10.1016/j.epsl.2010.11.044.

Behr, W.M., and Platt, J.P. 2014. is strong : Implications for lithospheric mechanics. Geophysical Research Letters RESEARCH,: 8067–8075. doi:10.1002/2014GL061349.Received.

Bestmann, M., and Prior, D.J. 2003. Intragranular dynamic recrystallization in naturally deformed calcite marble: Diffusion accommodated grain boundary sliding as a result of subgrain rotation recrystallization. Journal of Structural Geology, **25**: 1597–1613. Elsevier Ltd. doi:10.1016/S0191-8141(03)00006-3.

Bilham, R. 2019. Himalayan earthquakes: A review of historical seismicity and early 21st century slip potential. Geological Society Special Publication, **483**: 423–482. doi:10.1144/SP483.16.

Bouchez, J.L. 1978. Preferred orientations of quartz 〈a〉 axes in some tectonites: kinematic inferences. Tectonophysics, **49**: T25–T30. Elsevier. doi:10.1016/0040-1951(78)90094-X.

Burbank, D.W., Beck, R.A., and Mulder, T. 1996. The Himalayan foreland basin. *In* The Tectonic Evolution of Asia. pp. 149–188. Available from http://www.academia.edu/download/36556000/burbank_Himalyan_Foreland_1996_copy.pdf [accessed 22 March 2020].

Cross, A.J., Prior, D.J., Stipp, M., and Kidder, S. 2017. The recrystallized grain size piezometer for quartz: An EBSD-based calibration. Geophysical Research Letters, **44**: 6667–6674. doi:10.1002/2017GL073836.

Daniel, C.G., Hollister, L.S., Parrish, R.R., and Grujic, D. 2003. Exhumation of the main central thrust from lower crustal depths, Eastern Bhutan Himalaya. Journal of Metamorphic Geology, **21**: 317–334. Blackwell Publishing Inc. doi:10.1046/j.1525-1314.2003.00445.x.

Dasgupta, S., Bhutan, O.B.-T., and 1995, U. (n.d.). Jaishidanda formation. Geological Society of India Special …,.

Fossen, H. 2016. Structural Geology Second Edition. Available from www.cambridge.org [accessed 23 March 2020].

Gansser, A. 1964. Geology of the Himalayas. Interscience.

Gansser, A. 1983. Geology of the Bhutan Himalaya. Birkhäuser Verlag.

Godin, L., Grujic, D., Law, R.D., and Searle, M.P. 2006. Channel flow, ductile extrusion and exhumation in continental collision zones: An introduction. Geological Society Special Publication, **268**: 1–23. doi:10.1144/GSL.SP.2006.268.01.01.

Grujic, D., Ashley, K.T., Coble, M.A., Coutand, I., Kellett, D.A., Larson, K.P., Whipp, D.M., Gao, M., and Whynot, N. 2020. Deformational Temperatures Across the Lesser Himalayan Sequence in Eastern Bhutan and Their Implications for the Deformation History of the Main Central Thrust. Tectonics, **39**. John Wiley & Sons, Ltd. doi:10.1029/2019TC005914.

Grujic, D., Hetényi, G., Cattin, R., Baruah, S., Benoit, A., Drukpa, D., and Saric, A. 2018. Stress transfer and connectivity between the Bhutan Himalaya and the Shillong Plateau. Tectonophysics, **744**: 322–332. Elsevier. doi:10.1016/j.tecto.2018.07.018.

Grujic, D., Warren, C.J., and Wooden, J.L. 2011. Rapid synconvergent exhumation of Miocene-aged lower orogenic crust in the eastern Himalaya. Lithosphere, **3**: 346–366. doi:10.1130/L154.1.

Halfpenny, A. 2010. Some important practical issues for the collection and manipulation of electron backscatter diffraction (EBSD) data from geological samples. Journal of the Virtual Explorer, **35**. doi:10.3809/jvirtex.2011.00272.

Hammer, P., Berthet, T., Hetényi, G., Cattin, R., Drukpa, D., Chophel, J., Lechmann, S., Moigne, N. Le, Champollion, C., and Doerflinger, E. 2013. Flexure of the India plate underneath the Bhutan Himalaya. Geophysical Research Letters, **40**: 4225–4230. doi:10.1002/grl.50793.

Heilbronner, R., and Kilian, R. 2017. The grain size(s) of Black Hills Quartzite deformed in the dislocation creep regime. Solid Earth Discussions,: 1–57. doi:10.5194/se-2017-30.

Heilbronner, R., and Tullis, J. 2006. Evolution of c axis pole figures and grain size during dynamic recrystallization: Results from experimentally sheared quartzite. Journal of Geophysical Research: Solid Earth, **111**: 1–19. doi:10.1029/2005JB004194.

Heim, A., and Gansser, A. 1939. Central Himalaya: Geological Observations of Swiss, 1939 Expedition (reprinted 1975).

Hetényi, G., Le Roux-Mallouf, R., Berthet, T., Cattin, R., Cauzzi, C., Phuntsho, K., and Grolimund, R. 2016. Joint approach combining damage and paleoseismology observations constrains the 1714 A.D. Bhutan earthquake at magnitude 8 ± 0.5. Geophysical Research Letters, **43**: 10,695-10,702. doi:10.1002/2016GL071033.

Hirth, G., Teyssier, C., and Dunlap, W.J. 2001. An evaluation of quartzite flow laws based on comparisons between experimentally and naturally deformed rocks. International Journal of Earth Sciences, **90**: 77–87. doi:10.1007/s005310000152.

Hirth, G., and Tullis, J. 1992. Dislocation creep regimes in quartz aggregates. Journal of Structural Geology, **14**: 145–159. doi:10.1016/0191-8141(92)90053-Y.

Hodges, K. V. 2000. Tectonics of the Himalaya and Southern Tibet from two perspectives. Bulletin of the Geological Society of America, **112**: 324–350. doi:10.1130/0016-7606(2000)112<324:TOTHAS>2.0.CO;2.

Jessell, M.W. 1987. Grain-boundary migration microstructures in a naturally deformed quartzite. Journal of Structural Geology, **9**: 1007–1014. doi:10.1016/0191-8141(87)90008-3.

Kidder, S., Hirth, G., Avouac, J.P., and Behr, W. 2016. The influence of stress history on the grain size and microstructure of experimentally deformed quartzite. Journal of Structural Geology, **83**: 194–206. Elsevier Ltd. doi:10.1016/j.jsg.2015.12.004.

Kirby, S.H. 1980. Rheology of the lithosphere. U.S. national report to international union of geodesy and geophysics

Landry, K.R., Coutand, I., Whipp, D.M., Grujic, D., and Hourigan, J.K. 2016. Late Neogene tectonically driven crustal exhumation of the Sikkim Himalaya: Insights from inversion of multithermochronologic data. Tectonics, **35**: 833–859. Blackwell Publishing Ltd. doi:10.1002/2015TC004102.

Larson, K., Cottle, J., Lederer, G., and Rai, S.M. 2017. Defining shear zone boundaries using fabric intensity gradients: An example from the east-central Nepal Himalaya. Geosphere, **13**: 771–781. Geological Society of America. doi:10.1130/GES01373.1.

Law, R.D., Stahr, D.W., Francsis, M.K., Ashley, K.T., Grasemann, B., and Ahmad, T. 2013. Deformation temperatures and flow vorticities near the base of the greater Himalayan series, Sutlej valley and Shimla klippe, NW India. Journal of Structural Geology, **54**: 21–53. Elsevier Ltd. doi:10.1016/j.jsg.2013.05.009.

Lister, G.S. 1977, April 20. Discussion: Crossed-girdle c-axis fabrics in quartzites plastically deformed by plane strain and progressive simple shear. doi:10.1016/0040-1951(77)90087-7.

Little, T.A., Prior, D.J., Toy, V.G., and Lindroos, Z.R. 2015. The link between strength of lattice preferred orientation, second phase content and grain boundary migration: A case study from the Alpine Fault zone, New Zealand. Journal of Structural Geology, **81**: 59–77. Elsevier Ltd. doi:10.1016/j.jsg.2015.09.004.

Long, S., McQuarrie, N., Tobgay, T., Rose, C., Gehrels, G., and Grujic, D. 2011. Tectonostratigraphy of the lesser Himalaya of Bhutan: Implications for the along-strike stratigraphic continuity of the northern Indian margin. Bulletin of the Geological Society of America, **123**: 1406–1426. doi:10.1130/B30202.1.

Mallyon, D. 2014. Tectonic and Climatic controls on the Growth and Shape of the Himalayan Foreland Fold-and-Thrust Belt: A Numerical Study.

Martin, A.J. 2017a, September 1. A review of definitions of the Himalayan Main Central Thrust. Springer Verlag. doi:10.1007/s00531-016-1419-8.

Martin, A.J. 2017b, September 1. A review of Himalayan stratigraphy, magmatism, and structure. Elsevier Inc. doi:10.1016/j.gr.2017.04.031.

McQuarrie, N., Robinson, D., Long, S., Tobgay, T., Grujic, D., Gehrels, G., and Ducea, M. 2008. Preliminary stratigraphic and structural architecture of Bhutan: Implications for the along strike architecture of the Himalayan system. Earth and Planetary Science Letters, **272**: 105–117. doi:10.1016/j.epsl.2008.04.030.

Najman, Y. 2006. The detrital record of orogenesis: A review of approaches and techniques used in the Himalayan sedimentary basins. Earth-Science Reviews, **74**: 1–72. Elsevier B.V. doi:10.1016/j.earscirev.2005.04.004.

Najman, Y., Appel, E., Boudagher-Fadel, M., Bown, P., Carter, A., Garzanti, E., Godin, L., Han, J., Liebke, U., Oliver, G., Parrish, R., and Vezzoli, G. 2010. Timing of India-Asia collision: Geological, biostratigraphic, and palaeomagnetic constraints. Journal of Geophysical Research: Solid Earth, **115**. Blackwell Publishing Ltd. doi:10.1029/2010JB007673.

Nelson, K.D., Zhao, W., Brown, L.D., Kuo, J., Che, J., Liu, X., Klemperer, S.L., Makovsky, Y., Meissner, R., Mechie, J., Kind, R., Wenzel, F., Ni, J., Nabelek, J., Chen, L., Tan, H., Wei, W., Jones, A.G., Booker, J., Unsworth, M., Kidd, W.S.F., Hauck, M., Alsdorf, D., Ross, A., Cogan, M., Wu, C., Sandvol, E., and Edwards, M. 1996. Partially molten middle crust beneath southern Tibet: Synthesis of project INDEPTH results. Science, **274**: 1684–1685. doi:10.1126/science.274.5293.1684.

Nevitt, J.M., Warren, J.M., and Pollard, D.D. 2017. Testing constitutive equations for brittle-ductile deformation associated with faulting in granitic rock. Journal of Geophysical Research: Solid Earth, **122**: 6269–6293. Blackwell Publishing Ltd. doi:10.1002/2017JB014000.

Okudaira, T., Takeshita, T., Hara, I., and Ando, J. ichi. 1995. A new estimate of the conditions for transition from basal 〈a〉 to prism [c] slip in naturally deformed quartz. Tectonophysics, **250**: 31–46. Elsevier. doi:10.1016/0040-1951(95)00039-4.

Passchier, C.W., and Trouw, R.A.J. 2005. Microtectonics. *In* Microtectonics. Springer Berlin Heidelberg. doi:10.1007/3-540-29359-0.

Rogers, G. 2007. Subduction Zone: The Chatter of Silent Slip Episodic Tremor and Slip on the Cascadia. doi:10.1126/science.1084783.

Rutter, E.H., and Brodie, K.H. 2004. Experimental intracrystalline plastic flow in hot-pressed synthetic quartzite prepared from Brazilian quartz crystals. Journal of Structural Geology, **26**: 259–270. doi:10.1016/S0191-8141(03)00096-8.

Schmid, S.M., and Casey, M. 1986. Complete fabric analysis of some commonly observed quartz C-axis patterns. American Geophysical Union (AGU). pp. 263–286. doi:10.1029/gm036p0263.

Scholz, C.H. 1988. The brittle-plastic transition and the depth of seismic faulting. Geologische Rundschau, **77**: 319–328. doi:10.1007/BF01848693.

Searle, M.P., Law, R.D., Godin, L., Larson, K.P., Streule, M.J., Cottle, J.M., and Jessup, M.J. 2008. Defining the Himalayan Main Central Thrust in Nepal. Journal of the Geological Society, **165**: 523–534. doi:10.1144/0016-76492007-081.

SEARLE, M.P., LAW, R.D., GODIN, L., LARSON, K.P., STREULE, M.J., COTTLE, J.M., and JESSUP, M.J. 2008. Defining the Himalayan Main Central Thrust in Nepal. Journal of the Geological Society, **165**: 523–534. doi:10.1144/0016-76492007-081.

Sibson, R.H. 1982. Fault zone models, heat flow, and the depth distribution of earthquakes in the continental crust of the United States. <I>Bull. Seism. Soc. Amer</I>., **72**: 151–163.

Sibson, R.H. 1983. Continental fault structure and the shallow earthquake source. Journal of the Geological Society, **140**: 741–767. doi:10.1144/gsjgs.140.5.0741.

Skemer, P., Katayama, I., Jiang, Z., and Karato, S.I. 2005. The misorientation index: Development of a new method for calculating the strength of lattice-preferred orientation. Tectonophysics, **411**: 157–167. doi:10.1016/j.tecto.2005.08.023.

Starnes, J.K., Long, S.P., Gordon, S.M., Zhang, J., and Soignard, E. 2020. Using quartz fabric intensity parameters to delineate strain patterns across the Himalayan Main Central thrust. Journal of Structural Geology, **131**: 103941. Elsevier Ltd. doi:10.1016/j.jsg.2019.103941.

Stipp, M., Stünitz, H., Heilbronner, R., and Schmid, S.M. 2002. The eastern Tonale fault zone: A “natural

laboratory" for crystal plastic deformation of quartz over a temperature range from 250 to 700 °C. Journal of Structural Geology, **24**: 1861–1884. doi:10.1016/S0191-8141(02)00035-4.

Tokle, L., Hirth, G., and Behr, W.M. 2019. Flow laws and fabric transitions in wet quartzite. Earth and Planetary Science Letters, **505**: 152–161. Elsevier B.V. doi:10.1016/j.epsl.2018.10.017.

Toy, V.G., Prior, D.J., and Norris, R.J. 2008. Quartz fabrics in the Alpine Fault mylonites: Influence of pre-existing preferred orientations on fabric development during progressive uplift. doi:10.1016/j.jsg.2008.01.001.

Vermeesch, P. 2012. On the visualisation of detrital age distributions. Chemical Geology, **312**–**313**: 190–194. doi:10.1016/j.chemgeo.2012.04.021.

Vollmer, F.W. 1990. An application of eigenvalue methods to structural domain analysis. Bulletin of the Geological Society of America, **102**: 786–791. doi:10.1130/0016-7606(1990)102<0786:AAOEMT>2.3.CO;2.

Wech, A.G., and Creager, K.C. 2011. A continuum of stress, strength and slip in the Cascadia subduction zone. Nature Geoscience, **4**. doi:10.1038/NGEO1215.

Yin, A. 2006. Cenozoic tectonic evolution of the Himalayan orogen as constrained by along-strike variation of structural geometry, exhumation history, and foreland sedimentation. Earth-Science Reviews, **76**: 1–131. Elsevier B.V. doi:10.1016/j.earscirev.2005.05.004.

Appendix A: Supplementary EBSD Analysis

A.1 Orientation grain maps, in the IPF colouring scheme (Figure 3.6).

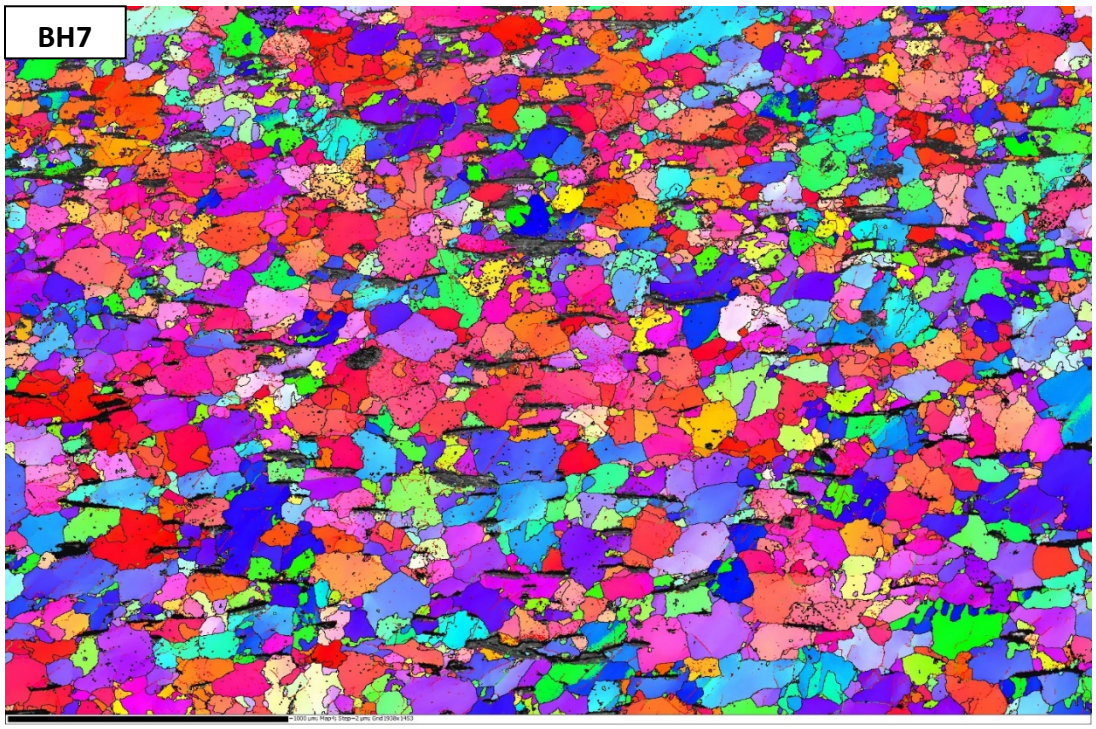

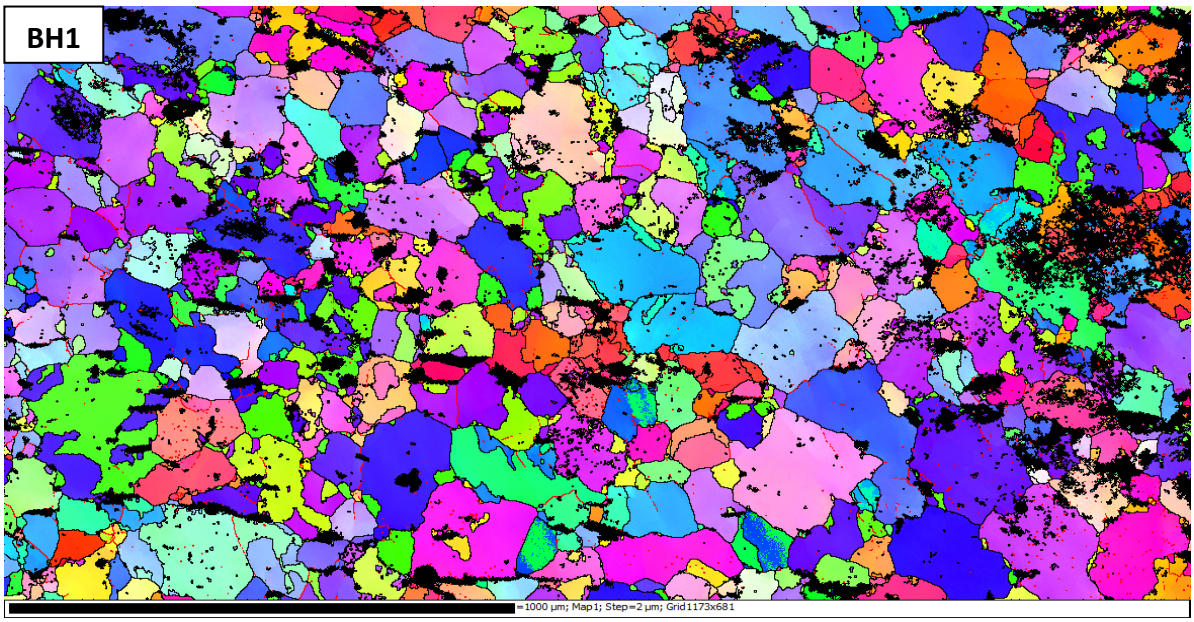


BH805

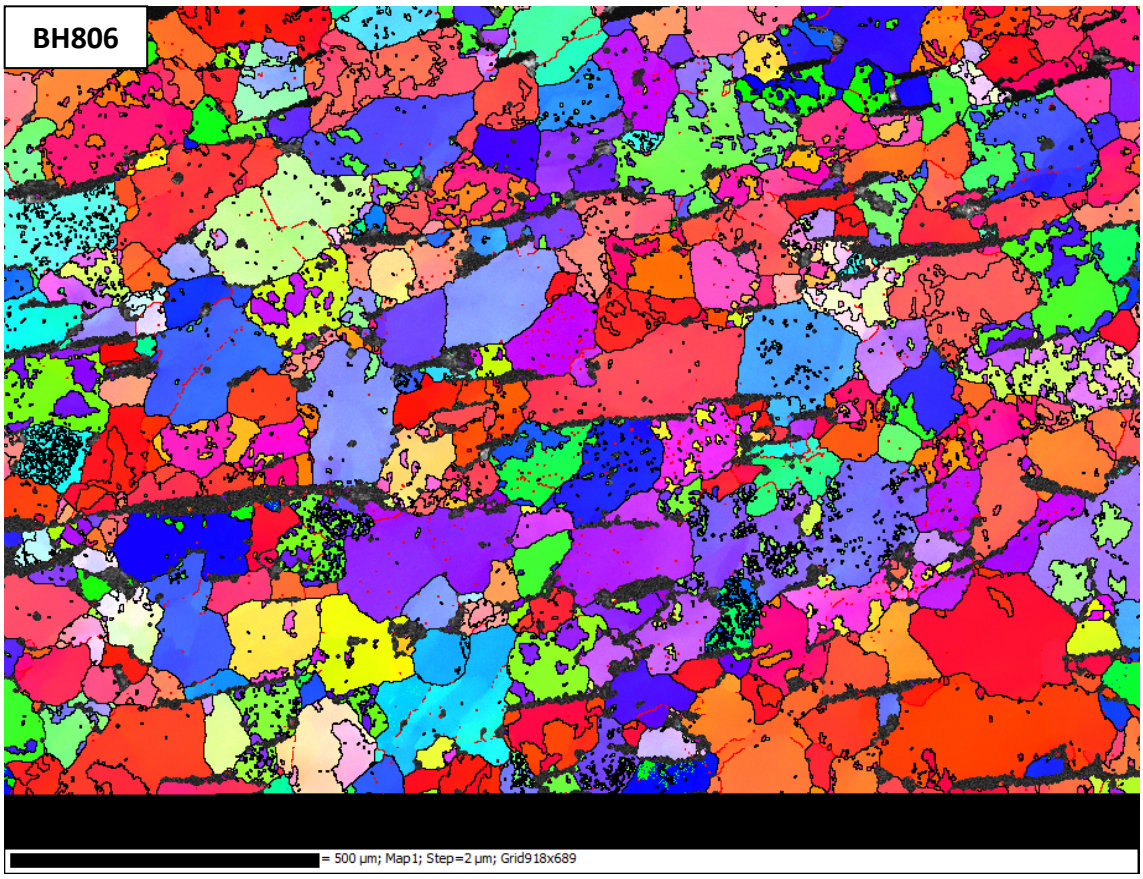
BH806
= 500 µm; Map1; Step=2 µm; Grid918x689

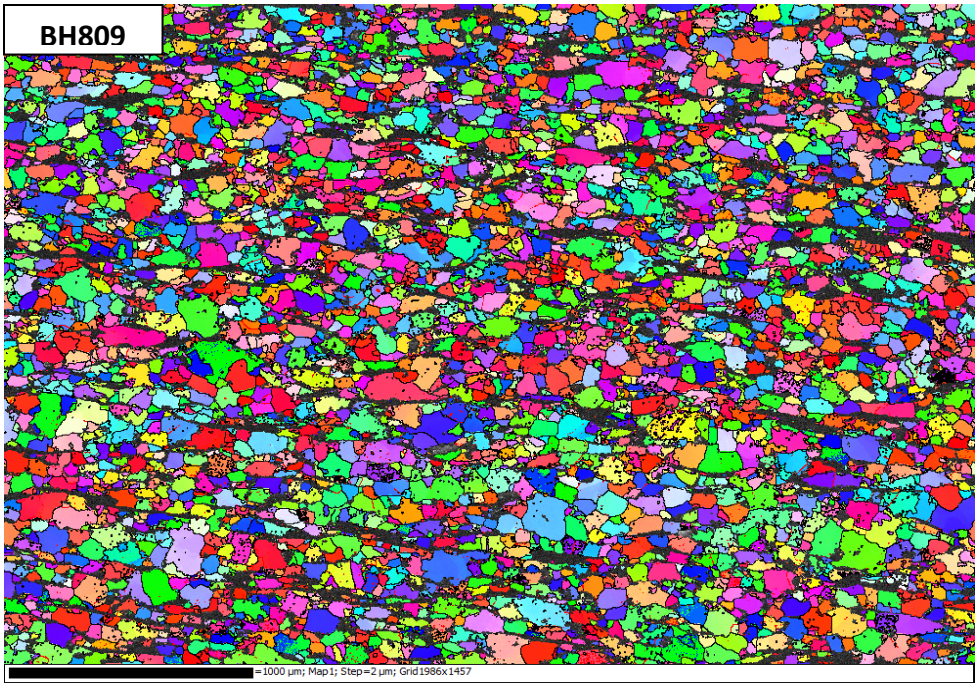
BH809
=1000 µm; Map1; Step=2 µm; Grid1986x1457

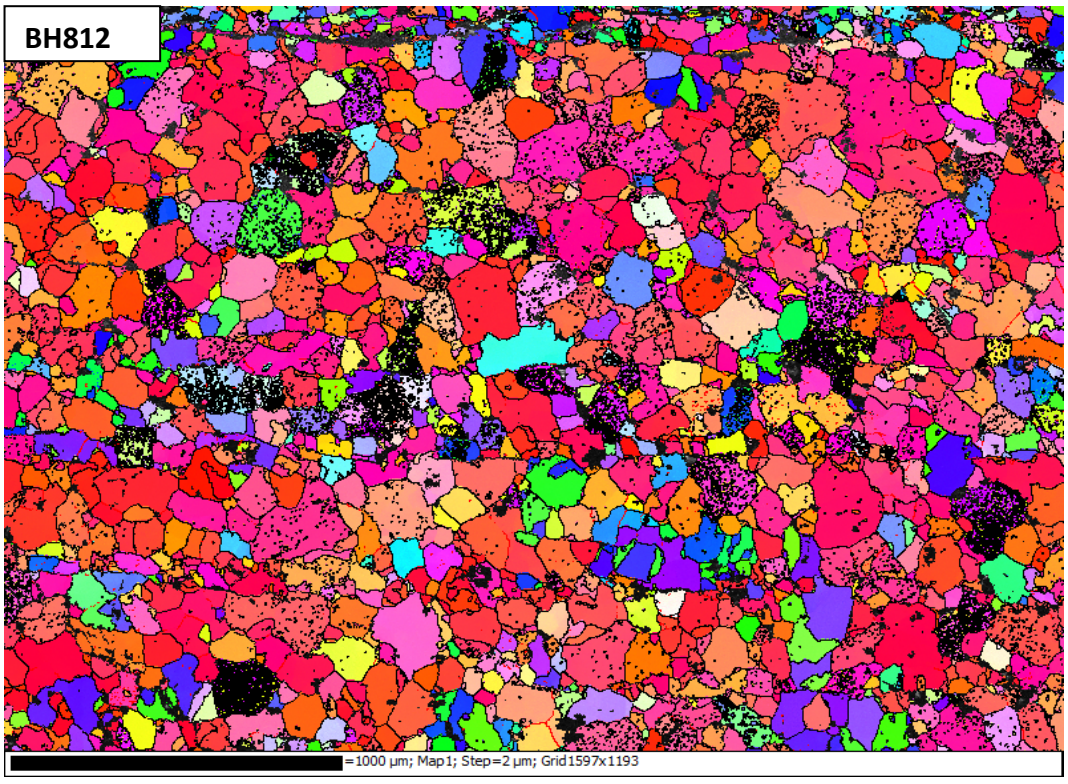
BH812
=1000 µm; Map1; Step=2 µm; Grid1597x1193

A.2 Crystallographic Preferred Orientation Pole Figures. Full dataset CPOs present the orientation of one point per grain.

BH7 Full Dataset

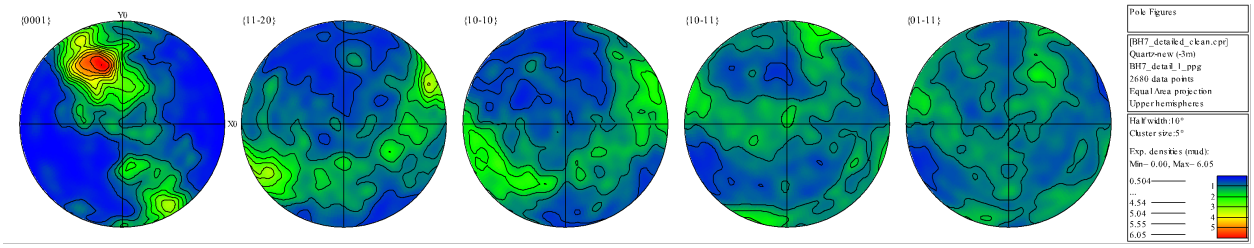

BH7 Large Grains

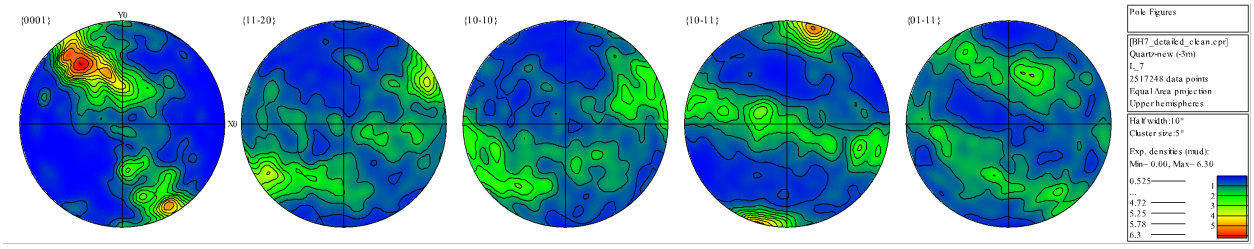

BH7 Small Grains

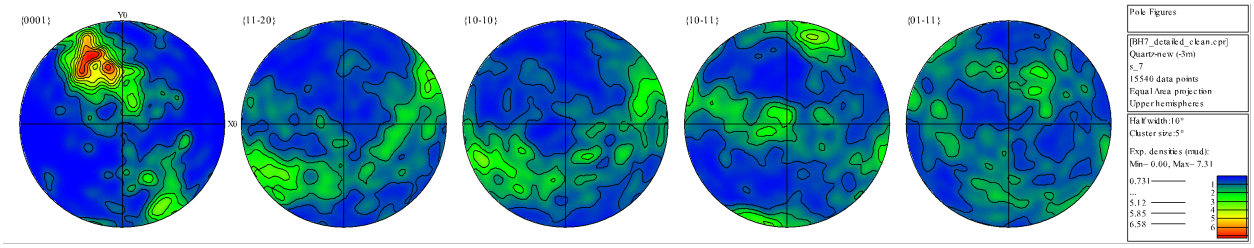

BH1 Full Dataset

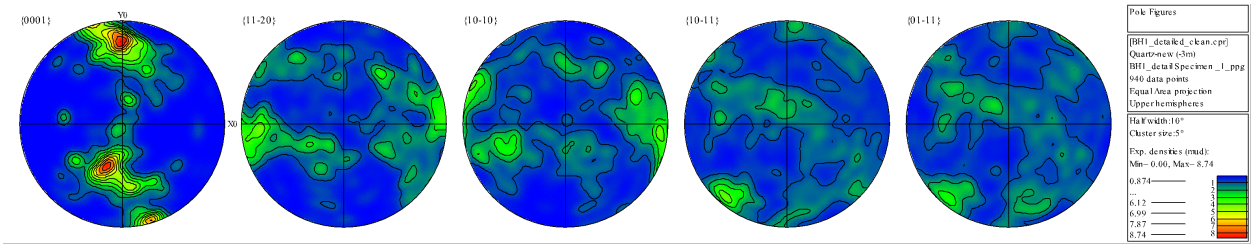

BH1 Large Grains

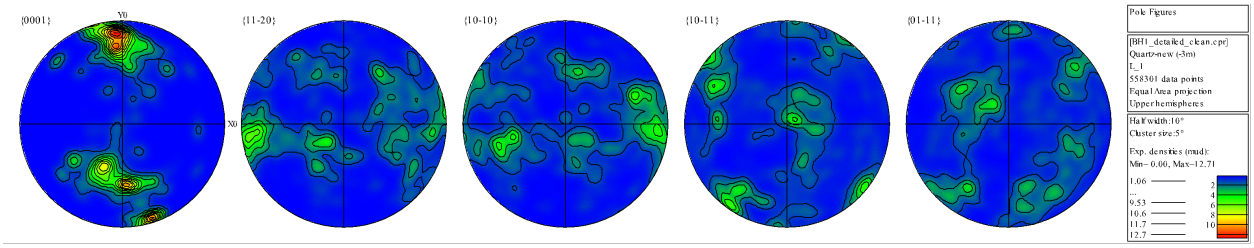

BH1 Small Grains

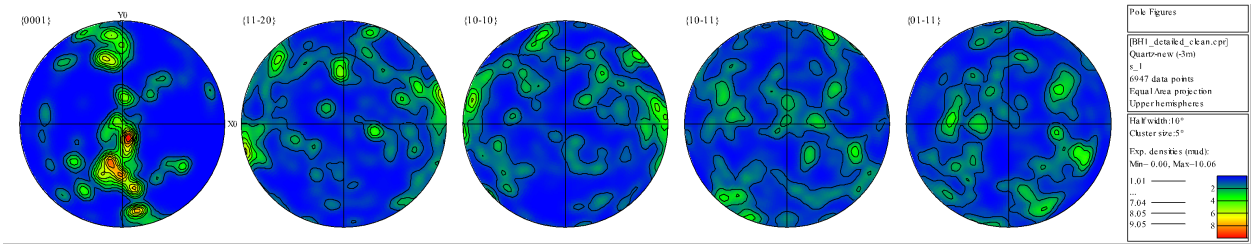

BH805 Full Dataset

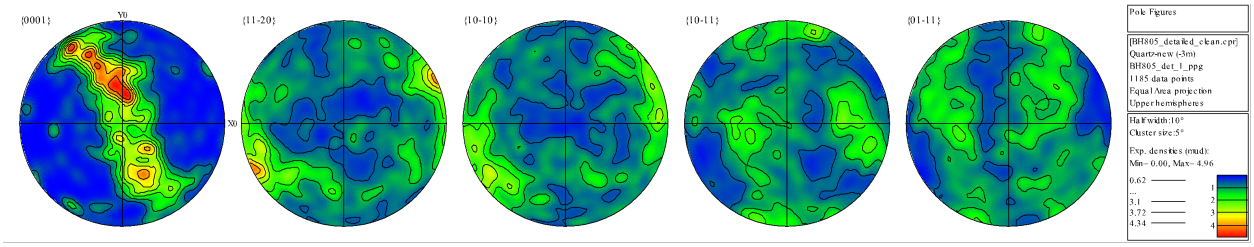

BH805 Large Grains

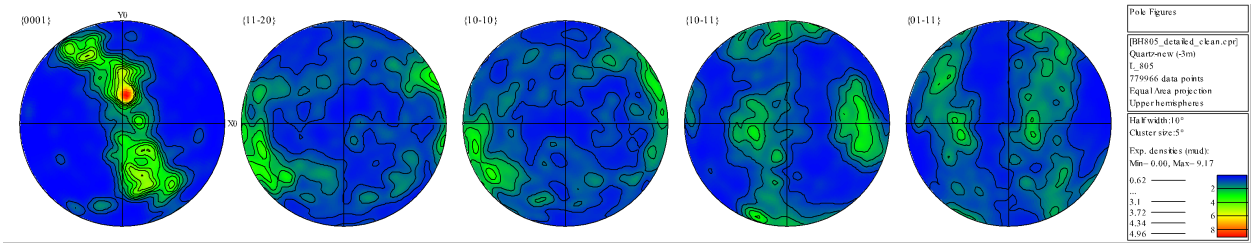

BH805 Small Grains

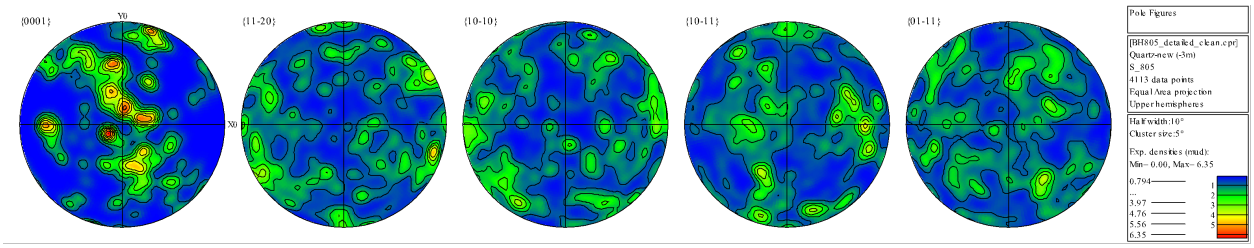

BH806 Full Dataset

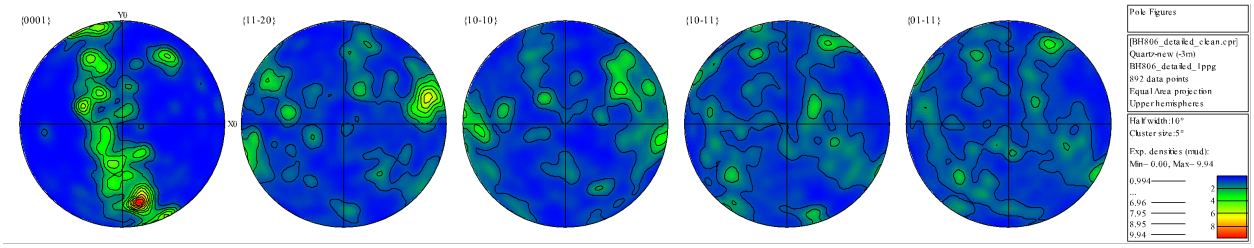

BH806 Large Grains

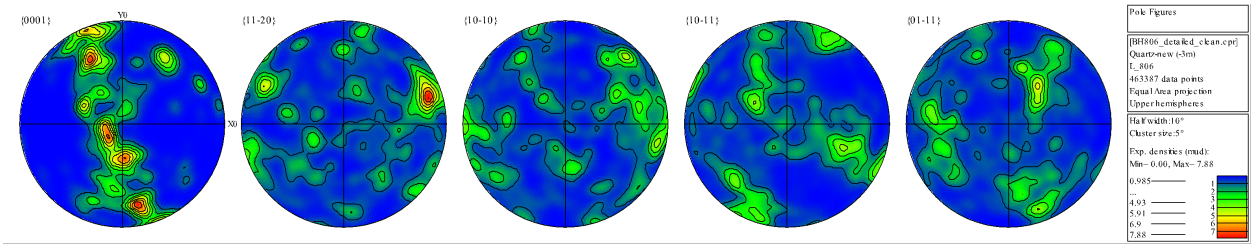

BH806 Small Grains

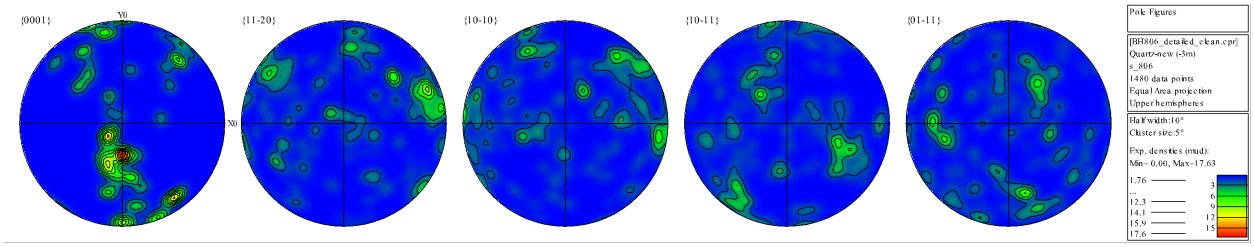

BH809 Full Dataset

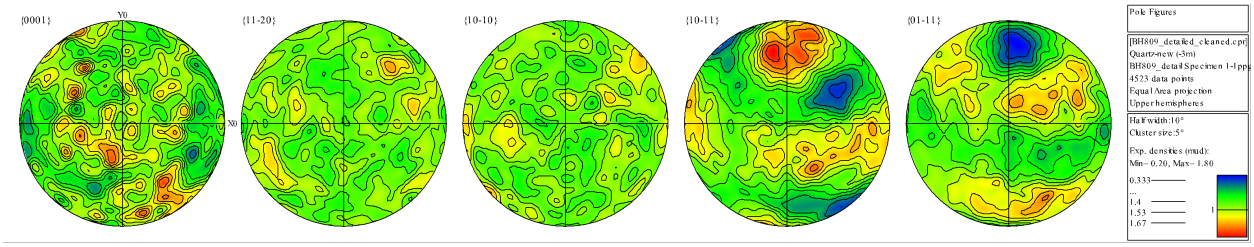

BH809 Large Grains

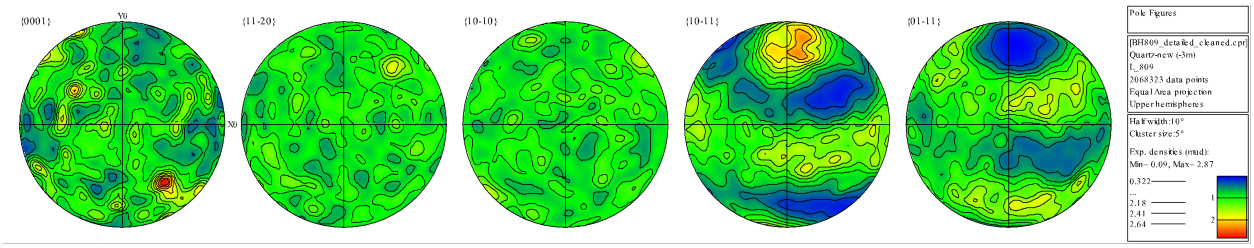

BH809 Small Grains

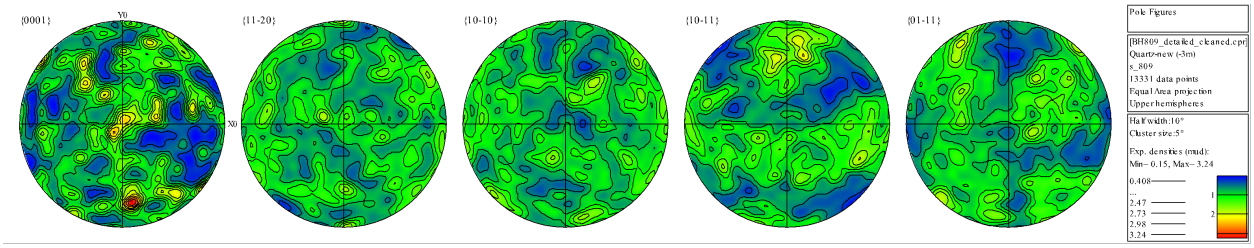

BH812 Full Dataset

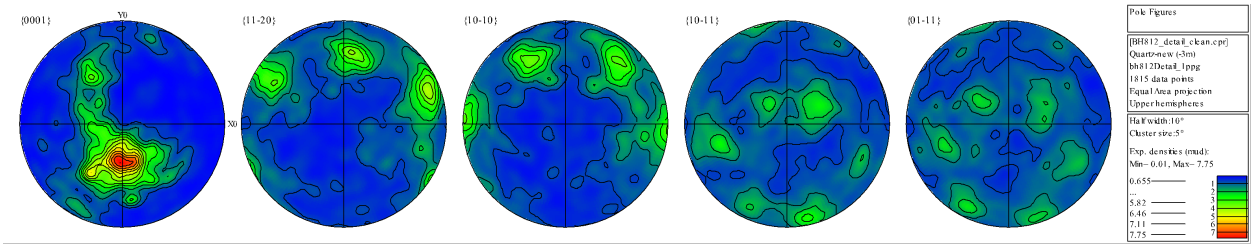

BH812 Large Grains

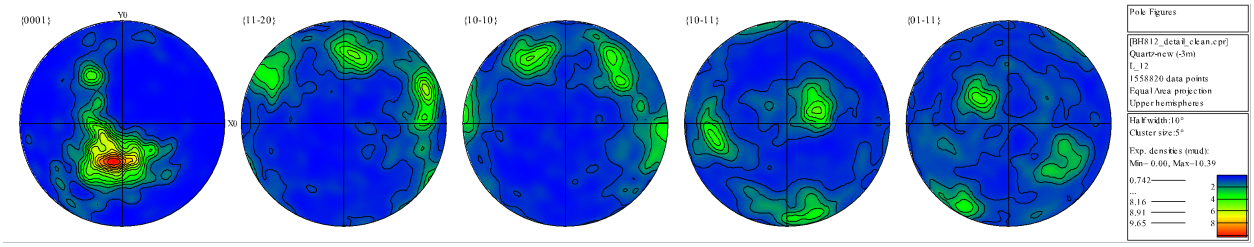

BH812 Small Grains

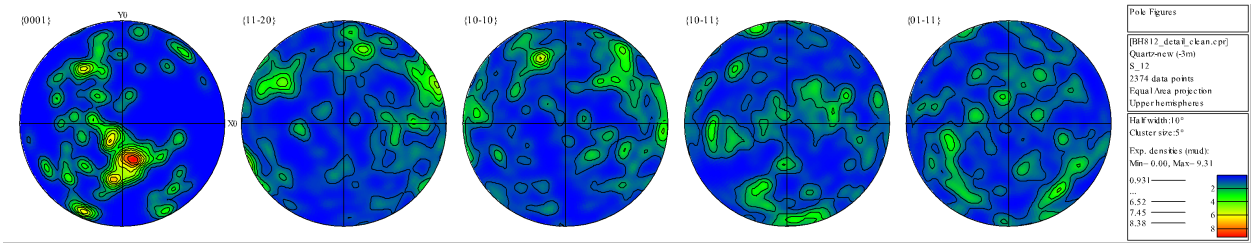

Appendix B: Population Density Plots

Sample BH7 (n=1509)

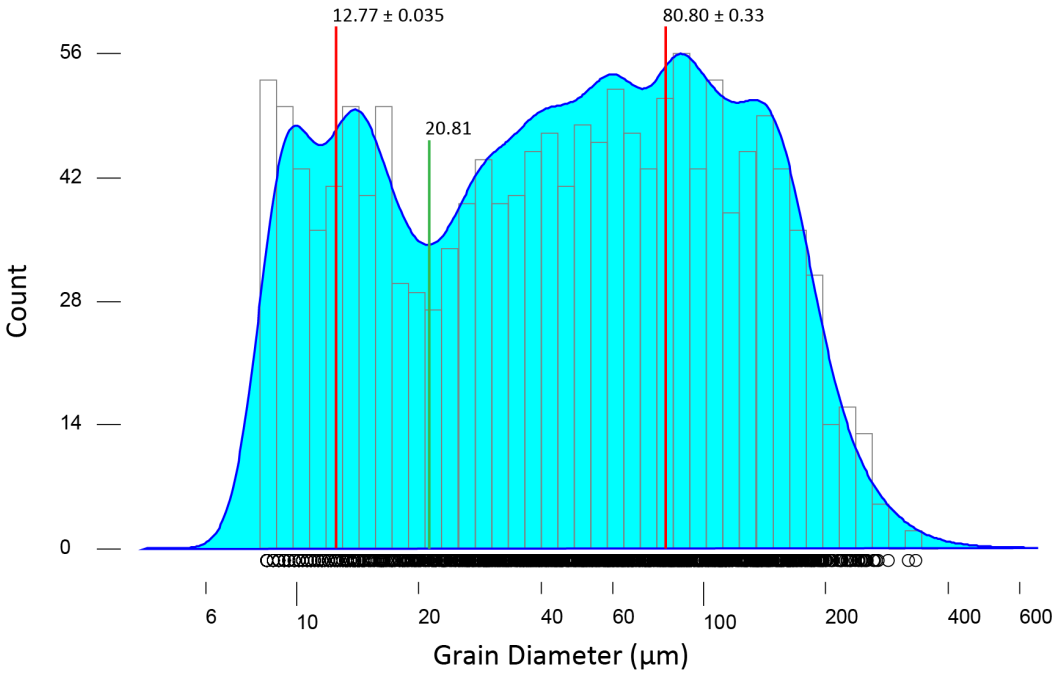

Sample BH1 (n=397)

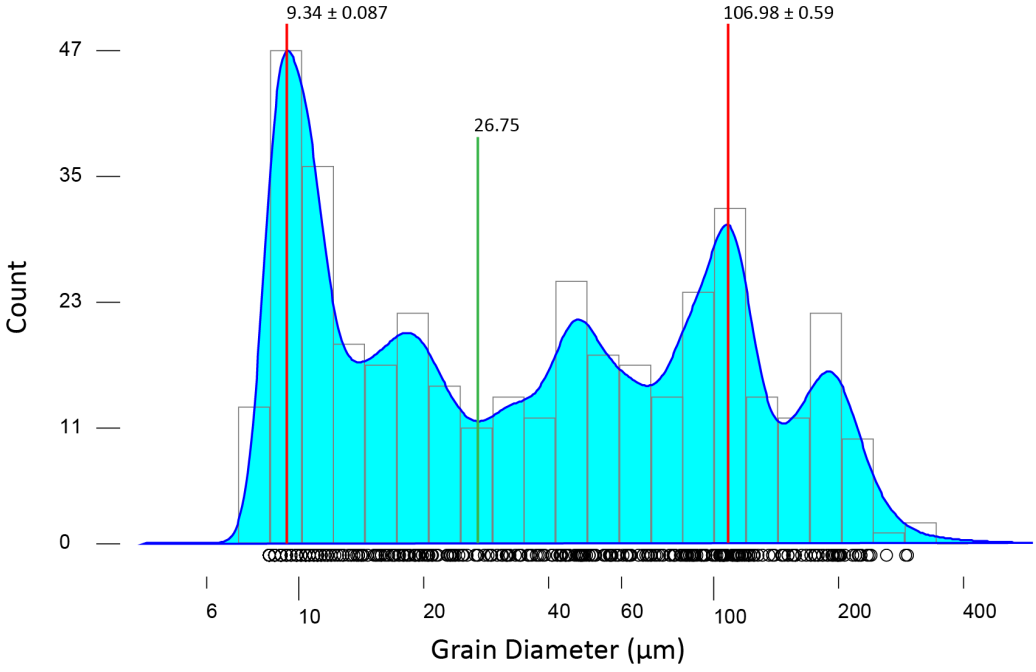

Sample BH805 (n=878)

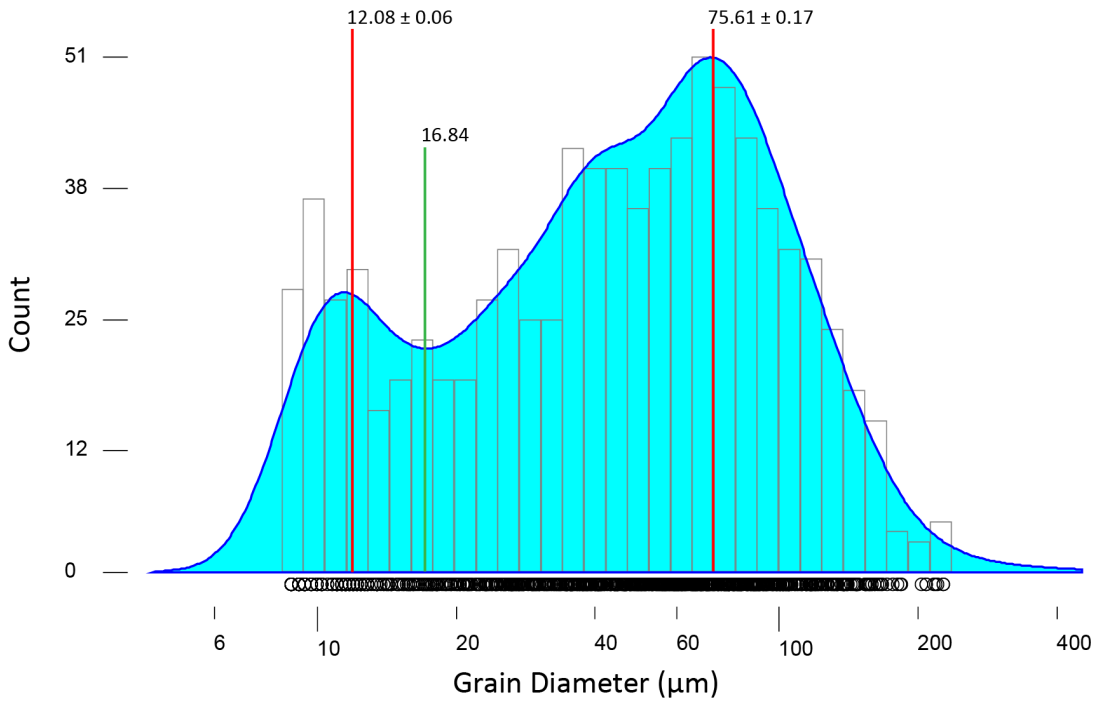

Sample BH806 (n=316)

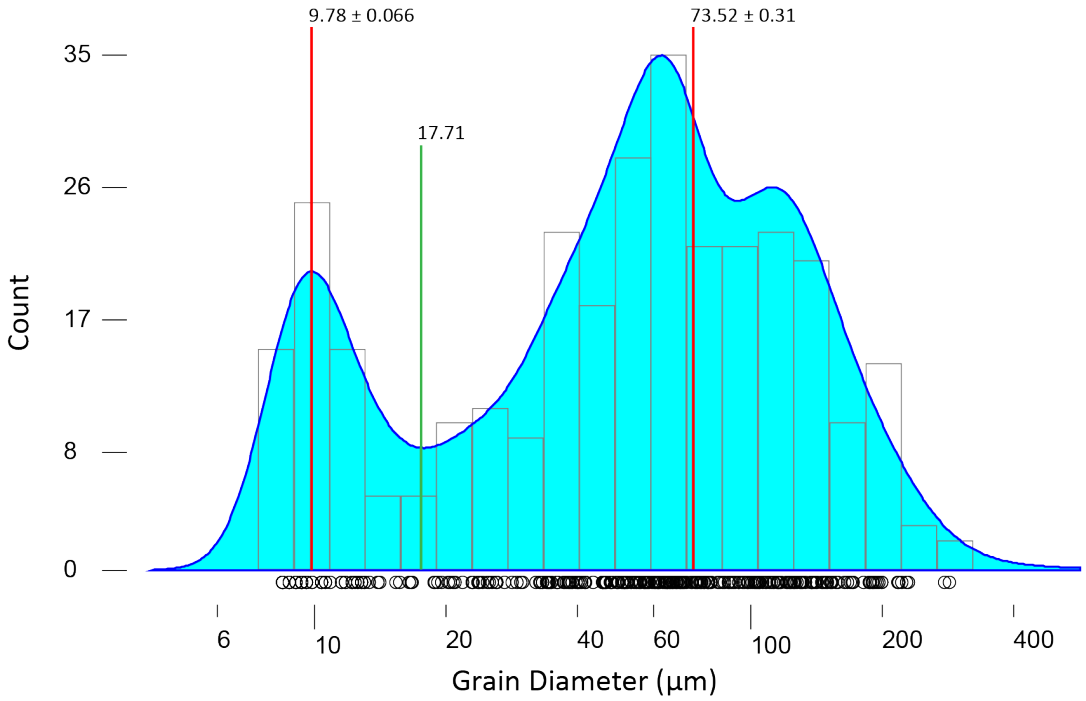

Sample BH809 (n=4021)

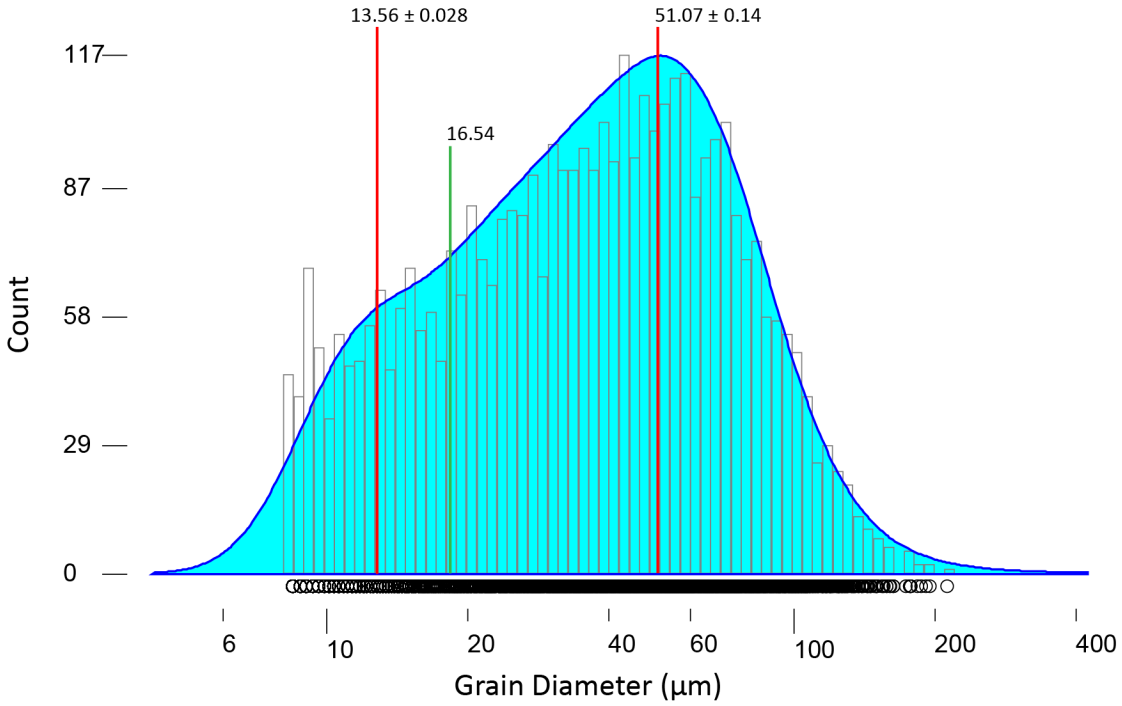

Sample BH12 (n=996)

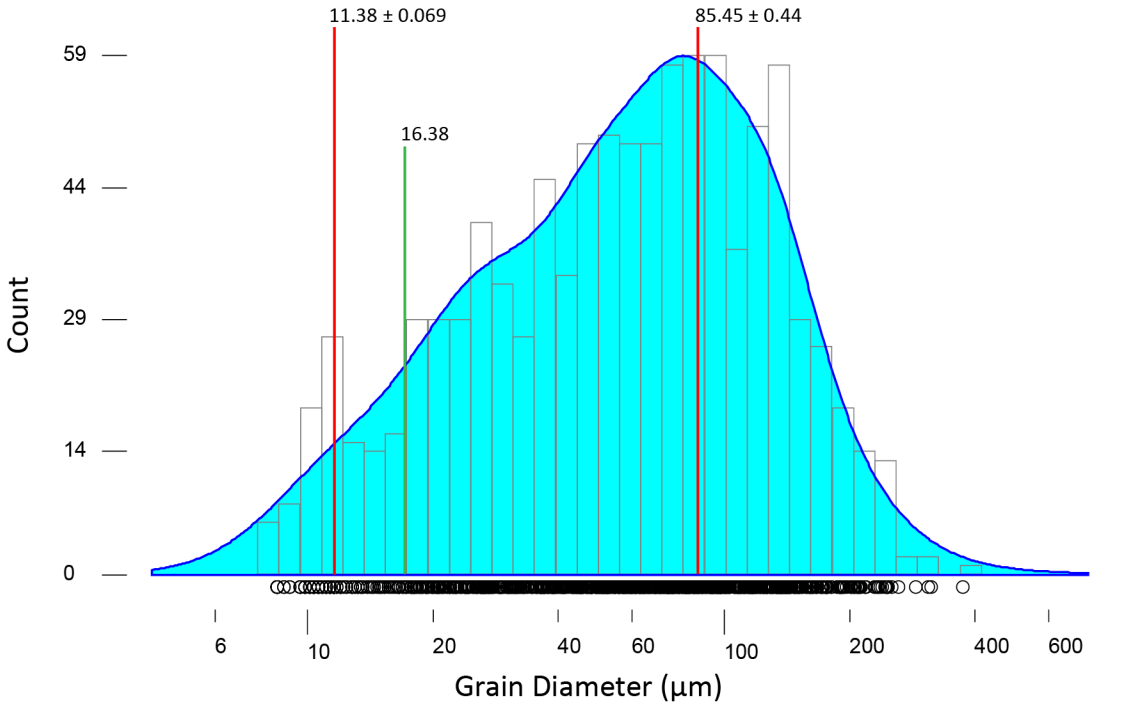

Appendix C: Flow Stress and Strain Rate Calculations

Table C.1. The relevant parameters for the differential stress calculation and the strain rate calculation using the Hirth et al. (2001) quartz flow law. Grain size is the mean grain diameter for the population of interest (large or small grains) of each sample. Uncertainty of differential stress in MPa is calculated from equation 3. Temperature and pressure values were utilized to constrain water fugacity required for the strain rate calculation (equation 4).

	Sample	Grain size (d, μm)	d Error	Diff. Stress (σ, MPa)	Uncertainty of σ (MPa)	T min (°C)	T Error	Pressure (kbar)	*f*H2O (MPa)	Strain Rate (ε, s^{-1})
Large Grain Populations	7	12.77	0.035	90.86	41.18	400.00	50	2.918	55.376	8.758E-15
	1	9.34	0.087	110.61	51.24	395.00	50	2.918	57.367	1.367E-14
	805	12.08	0.06	94.09	42.81	382.00	50	2.997	52.304	4.735E-15
	806	9.78	0.066	107.46	49.62	360.00	50	2.918	42.296	2.411E-15
	809	13.56	0.028	87.49	39.49	387.00	50	3.050	56.388	4.952E-15
	812	11.38	0.069	97.69	44.64	337.00	50	2.573	30.695	4.999E-16

	Sample	Grain Size (d, μm)	d Error	Diff. Stress (σ, MPa)	Uncertainty of σ (MPa)	T max (°C)	T Error	Pressure (kbar)	*f*H2O (MPa)	Strain Rate (ε, s^{-1})
Small Grain Populations	7	80.80	0.330	28.47	11.37	530	50	5.570	305.555	2.10E-12
	1	106.98	0.590	23.87	9.36	530	50	5.570	305.555	1.04E-12
	805	75.61	0.170	29.69	11.91	505	50	3.714	138.218	5.87E-13
	806	73.52	0.310	30.22	12.14	442.8	50	3.316	87.402	6.50E-14
	809	51.07	0.140	38.00	15.65	485.4	50	3.448	113.601	7.55E-13
	812	85.45	0.440	27.49	10.94	386.7	50	2.997	54.166	4.01E-15